UNIVERSITAT POLITÈCNICA DE VALÈNCIA

School of Aerospace Engineering and Industrial Design

A computational study on the aerodynamic behavior of a experimental flat plate propeller

Master's Thesis

Master's Degree in Aeronautical Engineering

AUTHOR: Ponce Soler, José Alberto

Tutor: Quintero Igeño, Pedro Manuel

ACADEMIC YEAR: 2023/2024

Master's Degree in Aeronautical Engineering

Final Master's Degree Project

Academic Year 2023-2024

A computational study on the aerodynamic behavior of an experimental flat plate propeller

Author: Ponce Soler, José Alberto

Supervisors: Quintero Igeño, Pedro Manuel
Fernández de la Infiesta, Álvaro

Valencia, 2024

A bird sitting on a tree is never afraid of the branch breaking,
because its trust is not on the branch but on its own wings.

Acknowledgements

To my supervisors, Pedro Quintero and Álvaro Fernández, for offering me their unwavering support and confidence during the development of this project. To all the people, students, and professors I have met over the years at the Universitat Politècnica de València and The Hong Kong University of Science and Technology, for teaching me so much inside and outside the classrooms. To all my friends from Lorca and university, for making these years a stage full of unforgettable memories and being there when I most needed them. To my wonderful girlfriend, Marta, for deciding to be by my side on this journey and all those to come. To my entire family, without whom nothing would make sense, especially my parents, Juan and Lucía, and my sister, Marien, for believing in me and continuously encouraging me to fly higher.

Thank you all for your support and helping me to become a better person every day.

Abstract

In the following report, the aerodynamic behavior of an experimental flat plate propeller is analysed through computational fluid dynamics (CFD) simulation, with the aim of understanding their efficiency and performance. The simulations involve a pseudo-steady approach to analyse the Reynolds independence on the characteristic curves of the propeller. Besides, different studies are developed in which the influence of certain parameters is analysed at several operating points. The results provide valuable insights into the aerodynamic behavior of flat plate propellers, and enable the identification of optimal design parameters for enhanced propeller performance. The findings of this study contribute to the broader understanding of flat plate propellers and their potential applications in various fields, such as unmanned aerial vehicles.

Keywords: UAV; Rotor; CFD; Aerodynamics; Propulsive efficiency.

Resumen

En el presente trabajo se analiza el comportamiento aerodinámico de una hélice experimental de placa plana mediante simulación de dinámica de fluidos computacional (CFD), con el objetivo de comprender su eficiencia y rendimiento. Las simulaciones utilizan un enfoque pseudoestacionario para analizar la independencia de Reynolds en las curvas características de la hélice. Además, se realizan diferentes estudios en los que se analiza la influencia de ciertos parámetros en varios puntos de operación. Los resultados proporcionan un conocimiento sobre el comportamiento aerodinámico de las hélices de placa plana y permiten identificar parámetros de diseño óptimos para mejorar el rendimiento de la hélice. Los hallazgos de este estudio contribuyen a una comprensión más amplia de las hélices de placa plana y sus posibles aplicaciones en diversos campos, tales como vehículos aéreos no tripulados.

Palabras clave: UAV; Rotor; CFD; Aerodinámica; Eficiencia propulsiva.

Table of Contents

List of Figures

List of Tables

Nomenclature

Latin symbols

$\dot{m}$	Mass flow rate
A	Rotor area
a	Speed of sound
AR	Aspect ratio
c	Chord
C_d	Drag force coefficient
C_l	Lift force coefficient
C_P	Power coefficient
C_Q	Torque coefficient
C_T	Trust force coefficient
CFL	Courant number
D	Rotor diameter
$error$	Relative error of the mesh
F	Prandtl's tip-loss factor
h	Thickness
J	Advance ratio
k	Turbulent kinetic energy
l_{ref}	Reference length
M	Mach number
n	Rotational velocity in rev/s
N_b	Number of blades
P	Power
p	Fluid pressure
Q	Torque

R	Rotor radius
r	Non-dimensional radial coordinate
R_{ij}	Reynolds Stress Tensor
Re	Reynolds number
s	Blade span
S_{ij}	Strain-rate tensor
T	Thrust
t	Time
u	Fluid velocity
U^+	Non-dimensional velocity
U_∞	Free stream velocity
u_τ	Friction velocity
U_P	Normal velocity
U_T	Tangential velocity
u_{ref}	Reference velocity
V_c	Climb velocity
v_i	Induced velocity at the rotor plane
w	Induced velocity at the slipstream
x, y, z	Position coordinates
y^+	Non-dimensional wall distance

Greek symbols

α	Aerodynamic angle of attack
Δt	Time step
Δx	Spatial step size
δ	Boundary layer thickness
δ_{ij}	Kronecker delta
η	Propeller efficiency
λ	Inflow ratio
μ	Dynamic viscosity
μ_t	Dynamic eddy viscosity
μ_v	Volume or second viscosity

ν	Kinematic viscosity
ν_t	Kinematic eddy viscosity
Ω	Rotational velocity
ω	Specific dissipation rate
ϕ_i	Induced angle of attack
ρ	Fluid density
σ	Rotor solidity
τ_w	Wall shear stress
τ_{ij}	Stress tensor
θ	Pitch angle
ε	Turbulent dissipation range

Abbreviations

BEMT	Blade Element Momentum Theory
BET	Blade Element Theory
BL	Boundary layer
CFD	Computational Fluid Dynamics
DES	Detached Eddy Simulation
DNS	Direct Numerical Simulation
FDM	Finite Differences Method
FEM	Finite Element Method
FVM	Finite Volumes Method
LES	Large Eddy Simulation
MRF	Moving Reference Frame
NSE	Navier-Stokes Equations
PISO	Pressure-Implicit with Splitting of Operators
RANS	Reynolds-Averaged Navier-Stokes
RBM	Rigid Body Motion
SDG	Sustainable Devolpment Goals
SIMPLE	Semi-Implicit Method for Pressure-Linked Equations
SST	Shear Stress Transport

Chapter 1

Introduction

1.1 Historical background

Propellers play a pivotal role in the aeronautical sector by converting rotational energy from engines into thrust. This fundamental component is essential for the operation of various aircraft, from helicopters to small private planes and large commercial airliners and even certain types of drones. The efficiency and effectiveness of propellers directly influence an aircraft's performance, including its speed, fuel consumption, and overall flight stability. The study and continuous improvement of propeller technology are vital for several reasons, including enhancing fuel efficiency, reducing noise, and improving overall performance.

Flat plate propellers, characterized by their simplicity in geometry, have been a subject of interest in both experimental and computational studies. One work in this area was conducted by Yu et al. (2013) [1], who investigated the aerodynamic performance of cycloidal propellers with flat plate airfoil through experiments and CFD. Their study provided fundamental insights into the interaction of the shedding vortexes and the thrust generation. The use of CFD for propeller simulations has become increasingly prevalent with the advent of high-performance computing. Notable work in this domain includes the study by Gaggero et al. (2017) [2], who utilized STAR-CCM+ to simulate the flow around a marine propeller. Their objectives were to validate CFD results against experimental data and open-source codes. Their findings underscored the capability of CFD to accurately predict propeller performance, provided that appropriate turbulence models and mesh resolutions are employed. Another significant contribution was made by Wang et al. (2020) [3], who conducted a comprehensive study on the comparison of the propeller wake using CFD and experiments. They successfully demonstrated that CFD matches overall trends well, mainly for the averaged flow field. More recently, Liu et al. (2023) [4] performed a comparison study on the aerodynamic performance of rotating propellers by means of CFD simulations, blade element momentum theory (BEMT) and wind tunnel tests, to explore their potential in low Reynolds number applications, such as small unmanned aerial vehicles (UAVs). Their results demonstrated that CFD simulations agree well with the experiments at all advance ratios, whereas the BEMT method was reliable particularly in low-speed regimes. This year, Xu et al. (2024) [5] employed the Moving Reference Frame (MRF) method within CFD to simulate the lift system of a Coaxial Contra-Rotating Propeller in eVTOL vehicles. In addition, they quantitatively analyzed aerodynamic performance indicators under different speed conditions.

The importance of propellers is becoming more pronounced with the evolution of aviation technology and market demands. As the industry moves towards more sustainable aviation solutions, electric and hybrid propulsion systems are gaining traction. Propellers are integral to these systems, offering a feasible and efficient means of thrust generation for electric aircraft. The study of propeller integration with these advanced propulsion systems is crucial for the future of sustainable aviation. The rise of urban air mobility, with the development of air taxis and other short-range aerial vehicles, relies heavily on efficient and quiet propeller technology. These vehicles are expected to operate in urban environments where noise and energy efficiency are paramount. Moreover, drones and UAVs are increasingly utilized for a variety of applications, including surveillance, delivery, and agricultural monitoring. Propeller efficiency directly affects the operational range and payload capacity of these UAVs, making the study and advancement of propeller technology critical for the expanding drone market.

(a) CityAirbus NextGen

(b) MQ-1B Predator

(c) DJI Phantom 4 Pro

Figure 1.1: Examples of UAVs. Images taken from [6], [7], [8].

Recently, at the *Institut Supérieur de l'Aéronautique et de l'Espace* (ISAE-SUPAERO) in Toulouse, an experimental test bench dedicated to the study of flexible blade rotors has been developed to conduct vibratory and aerodynamic analysis. In this study, various rotor blades with different mechanical characteristics were manufactured and analyzed to investigate their performance. The research focused on blades made from different materials, with variations in aspect ratio and thickness. The study was divided into two main tests. Firstly, a static test which primarily involved modal analysis of the blades.

The blades were set to vibrate to measure their excitation modes, aiming to understand the natural frequencies and vibration characteristics of the blades. Secondly, a rotor test, in which the blades were mounted in pairs on a rotor test bench and spun at different rotational speeds to observe phenomena such as flutter. The goal was to determine the rotational speeds at which aeroelastic instabilities occurred and to study the dynamic behavior of the blades in operation.

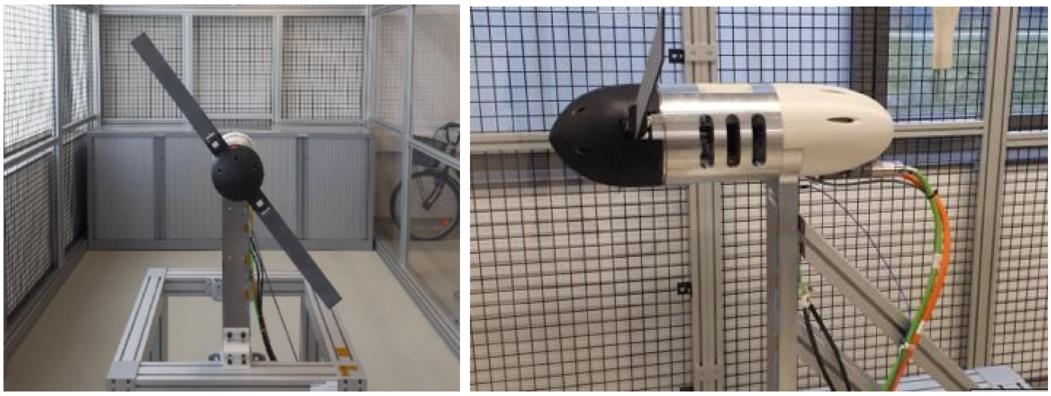
(a) Front view (b) Side view

Figure 1.2: Experimental test bench at ISAE-SUPAERO. Images taken from [9].

Similarly, on the same topic, an aeroelastic numerical model is being developed at the *Instituto Universitario de Investigación CMT - Clean Mobility and Thermofluids*, in the Universitat Politècnica de València. Among others, a fluid-structure interaction study was performed employing a beam element solver and artificial neural networks (ANN) to predict the aerodynamic behaviour [10]. This work focused on developing a aeroelastic reduced-order models (ROM) that compute the coupled phenomena without substantial accuracy losses. Besides, CFD-based studies are carried out aiming to obtain meaningful data that together with the experimental results, may serve as a data base to develop a simplified model that predicts flutter, and other aeroelastic instabilities, on any generic propeller blade.

1.2 Motivation and objectives

Modern advancements in propeller design contribute significantly to improved fuel efficiency. This is achieved through materials engineering, aerodynamic optimization, and the integration of advanced computational methods in the design process. More efficient propellers reduce fuel consumption, leading to lower operational costs and a smaller environmental footprint. Additionally, noise pollution is a critical concern, especially in densely populated areas near airports. Advances in propeller technology have led to designs that minimize noise, enhancing the quality of life for residents and complying with increasingly stringent noise regulations. Furthermore, new materials and aerodynamic shapes have improved propeller performance, allowing aircraft to achieve higher speeds and better maneuverability. This is particularly beneficial for military and emergency response aircraft, where speed and agility can be crucial.

Several key characteristics influence the performance of propellers, including blade design and shape, pitch, diameter, the number of blades, material, and rotational speed. The study of flat plate aerodynamics offers significant insights and benefits in the context of propeller design and general aerodynamic research. Flat plates provide a simplified model that aids in understanding fundamental aerodynamic principles. This foundational knowledge is crucial for comprehending more complex shapes and designs encountered in advanced propeller technology. Flat plates are often utilized as baseline models in experiments and simulations, providing a reference point for evaluating the aerodynamic performance of more intricate shapes. This benchmarking capability allows for precise adjustments and optimizations in propeller design. Additionally, studying flat plates facilitates flow visualization and analysis, including the examination of airflow patterns, boundary layer development, and turbulence.

The continuous advancements in CFD technologies and computational power provide unprecedented opportunities to explore and optimize propeller designs. Modern CFD tools, such as STAR-CCM+, allow for detailed analysis of complex flow phenomena, including turbulence, separation, and vortex formation, which are essential for understanding and improving propeller performance. Despite the significant progress made in the field, there remains a need for detailed studies that combine experimental and computational approaches to validate and enhance the understanding of propeller aerodynamics. The current study aims to fill this gap by providing a comprehensive CFD analysis of a propeller, and providing valuable insights into the optimal design and operational parameters for propellers.

The primary objective of the project is to develop a computational study to obtain insights on the aerodynamic performance of a flat plate bladed propeller. To do so, different CFD analyses are performed with the aim of determining the influence of certain parameters, on the thrust, efficiency, and other performance metrics, as well as to analyse the flow field around the propeller.

In order to achieve the main objective, a series of specific objectives for this project are proposed, which are:

- To define the fundamental concepts involving CFD simulations and rotor aerodynamics.
- To set up the different simulations in *STAR-CCM+* so as to obtain valuable insights on the performance of the propeller studied, while using low computational resources.
- To study the influence of the Reynolds number on the propeller's non-dimensional parameters characteristic curves.
- To analyse the effect of the propeller rotational speed on the thrust generated and to study the influence the blade thickness.
- To perform a parametric study of the pitch angle, analysing the trends of the performance parameters at different conditions.

1.3 Structure of the project

In order to achieve the aforementioned objectives, this project is structured into 6 chapters and 3 appendices, broken down as follows:

- In chapter 2, the fundamentals of Computational Fluid Dynamics are explored. Here, the equations that govern the fluid motion, together with turbulence and boundary layer theory in CFD are approached. Lastly, an overview of the numerical methods and algorithms used in CFD is done.
- Similarly, chapter 3 summarises the fundamentals of rotor aerodynamics. The three main theories that underlie the behaviour of propeller's aerodynamics are reviewed. Finally, a non-dimensional coefficients approach to analyse the performance of propellers is shown.
- The methodology followed along every CFD study performed in this project is found in chapter 4. Here, the main steps involving CFD simulations, such as computational domain, meshing strategy and setup, are explained in detail.
- In chapter 5, the results obtained from the previous CFD simulations are exposed and discussed.
- At chapter 6, the main conclusions of the current work will be depicted. Moreover, with the objective of improving the presented work, future lines of investigation are indicated.
- Finally, Appendix A correspond to the project scope statement; in Appendix B, the project budget is estimated; and Appendix C shows how the project is related to the Sustainable Development Goals (SDG).

Chapter 2

Fundamentals of Computational Fluid Dynamics

2.1 Introduction

Computational Fluid Dynamics (CFD) is a branch of fluid mechanics that uses numerical analysis and algorithms to solve and analyse problems involving fluid flows. It allows for the simulation of fluid motion and interaction with surfaces, providing insights that are often difficult or impossible to obtain through experimental methods alone. Applying CFD to real-world engineering problems presents numerous challenges, from ensuring computational efficiency and accuracy to managing complex geometries and data. Overcoming these challenges requires a combination of advanced numerical techniques, and expert knowledge in fluid dynamics. This chapter provides essential knowledge on the fundamentals of CFD simulations, including the fluid equations, turbulence models and boundary layer theory, as well as the numerical methods involved.

2.2 Flow Equations

Fluid dynamics is the branch of physics that studies the motion and behaviour of fluids, including liquids and gases. The fundamental principles that govern fluids behaviour are the conservation of mass (Equation 2.1), momentum (Equation 2.2) and energy (Equation 2.3) [11]. This is expressed by a set of mathematical equations, known as the *Navier-Stokes Equations* (NSE), which describe the motion of fluids in terms of velocity, pressure, and temperature. The equations for single-phase compressible flow, in their conservative form, can be expressed as

$$\frac{\partial \rho}{\partial t} + \frac{\partial \rho u_i}{\partial x_i} = 0 \tag{2.1}$$

$$\frac{\partial (\rho u_i)}{\partial t} + u_j \frac{\partial (\rho u_i)}{\partial x_j} = -\frac{\partial p}{\partial x_i} + \frac{\partial \tau_{ij}}{\partial x_j} + \rho f_i \tag{2.2}$$

$$\frac{\partial}{\partial t}\left[\rho\left(e + \frac{1}{2}u_i u_i\right)\right] + \frac{\partial}{\partial x_j}\left[\rho\left(e + \frac{1}{2}u_i u_i\right)u_j\right] = \frac{\partial}{\partial x_j}\left(-p u_j + \tau_{ij} u_i + k\frac{\partial T}{\partial x_i}\right) + \rho f_i u_i + Q \tag{2.3}$$

The terms appearing in the equations are $\rho = \rho(T, p)$, the local fluid density, and p, its pressure; $\boldsymbol{u}$, the flow velocity vector; $\boldsymbol{\tau}$, the stress tensor which accounts for the viscous effects and which, for Newtonian fluids (fluids that exhibit a viscosity that is exclusively dependent on temperature), can be expressed as Equation 2.4; $\mathbf{f}$ the vector of mass forces acting on the flow; $e = e(T, p)$, the local internal energy; k, thermal conductivity; T, temperature; and Q, the energy source term.

$$\tau_{ij} = \mu \left(\frac{\partial u_i}{\partial x_j} + \frac{\partial u_j}{\partial x_i} \right) + \left(\mu_v - \frac{2}{3}\mu \right) \frac{\partial u_k}{\partial x_k} \delta_{ij} \tag{2.4}$$

where μ is the dynamic viscosity, μ_v is the volume or second viscosity, and δ_{ij} is the Kronecker delta.

These equations are a set of partial differential equations that describe the relationship between different variables involved in the behaviour of a fluid in space and time, namely, density, velocity, pressure, and temperature [12]. The equations, described in their integral form, represent the behaviour of a fluid as a continuous system. However, solving these equations analytically is a complicated task that only has a solution in certain applications of elementary flows [13].

2.3 Turbulence

Turbulence is a chaotic state of the flow in which numerous vortexes are created and interact with each other. The largest eddies, with an integral length scale, l, are unstable and break up, transferring kinetic energy to smaller eddies. This break-up process continues with the smaller eddies transferring their energy to subsequent smaller eddies until the eddy motion becomes stable, dissipating the kinetic energy into heat by viscosity, in a phenomenon called energy cascade [14]. The phenomenon is commonly represented by the energy spectrum of the velocity field versus the wavenumber, κ, for the classification of eddies into three representative length scales. The transfer of energy goes from lower to higher wavenumbers. In the intermediate range of scales, the so-called inertial subrange, the energy spectrum does not depend on the kinematic viscosity of the fluid, but rather on the wavenumber and turbulent dissipation rate, ε.

The turbulent behaviour of the flow is related to the Reynolds number (Equation 2.5), which relates inertial and viscous forces acting on the flow. When the viscous effects are dominant, the flow is called laminar flow and the turbulent behaviour is negligible. For higher Reynolds numbers, the inertial forces are dominant and the flow becomes more chaotic, irregular and unsteady. Also, Kolmogorov length scales (smallest turbulent scales), η, become smaller following Equation 2.6 [15], requiring finer discretizations to capture them, which makes the computation process too expensive for practical applications.

$$Re = \frac{\rho u_{ref} l_{ref}}{\mu} \tag{2.5}$$

$$\frac{\eta}{l_{ref}} = Re^{-3/4} \tag{2.6}$$

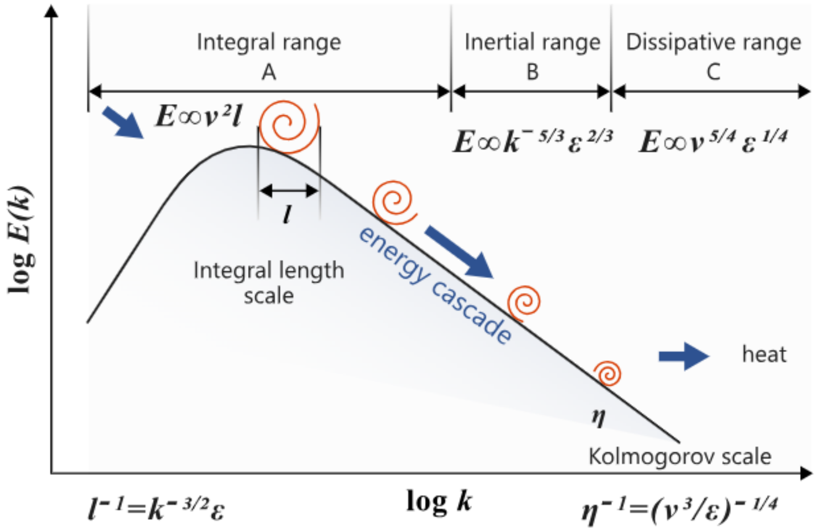

Figure 2.1: Turbulent energy cascade representation. Image taken from [16].

The method that solves the conservation equations completely is called DNS (*Direct Numerical Simulation*). This method gives the most accurate solution at the expense of an incredibly high computational cost, which even with the increasing improvements in computation, is not affordable in most cases.

In order to reduce the computational cost of solving the state of the flow, there have been developed turbulence models that solve the conservation equations by making use of several assumptions [17]. The methodologies that are more employed in computational fluid dynamics are *Large Eddy Simulation* (LES), *Reynolds-Averaged Navier-Stokes* (RANS) and *Detached Eddy Simulation* (DES).

- **LES**. LES method is an inherently transient approach that models Kolmogorov's scales and solves the scales in the inertial and integral range. This allows using a lower computational cost and the magnitude of the error in modelling is not substantial. LES equations are obtained by applying a spatial filtering operation, a temporal filtering operation, or both to the NSE. Then, each fluid variable, ϕ, may be split up into a filtered, $\hat{\phi}$, and sub-filtered portion, ϕ'.
- **RANS**. RANS methods consist of decomposing a fluid variable, ϕ, into the sum of its time average value plus a fluctuating part, $\phi = \overline{\phi} + \phi'$. This way, NSE can be expressed by modelling turbulence as fluctuations of time averages. This leads to a new term in the equations called *Reynolds Stress Tensor*, R_{ij}.
- **DES**. DES combines elements of the two previous models to capitalize on the strengths of both methods. Regions where the flow is attached and the turbulence scales are small are modeled using RANS. In regions away from the walls, where large-scale eddies dominate, the model switches to LES. While DES offers improvements in accuracy and efficiency over purely RANS or LES approaches, it requires careful grid design and parameter tuning to achieve optimal results. The performance of DES can be sensitive to the grid resolution, particularly in the transition regions [18].

2.3.1 RANS Turbulence Models

The incredible complexity of the fluid equations introduced above in this chapter makes their analytical resolution impossible. RANS methodology decreases the complexity of the problem by modelling the turbulence scales. The Reynolds decomposition simplifies the conservation equations by decomposing the instantaneous flow variables into their time average and fluctuating components. In this work the studies performed comprise incompressible flow, as the compressibility effects will not be analysed. Therefore, the averaged continuity and momentum equations result in

$$\frac{\partial \overline{u}_i}{\partial x_i} = 0 \tag{2.7}$$

$$\frac{\partial(\rho\overline{u}_i)}{\partial t} + \frac{\partial(\rho\overline{u}_i\overline{u}_j)}{\partial x_j} = -\frac{\partial(\overline{p}\delta_{ij})}{\partial x_j} + \frac{\partial\overline{\tau_{ij}}}{\partial x_j} + \frac{\partial R_{ij}}{\partial x_j} + f_i \tag{2.8}$$

where $\overline{p}$ is the average pressure, $\overline{\tau_{ij}}$ is the average shear stress tensor, and R_{ij} is the Reynolds stress tensor, which represents an additional stress due to the turbulent motions. Both tensors are defined as follows:

$$\overline{\tau_{ij}} = \mu\left(\frac{\partial\overline{u_i}}{\partial x_j} + \frac{\partial\overline{u_j}}{\partial x_i}\right) \tag{2.9}$$

$$R_{ij} = -\rho\overline{u_i'u_j'} \tag{2.10}$$

The existence of the Reynolds stress tensor introduces a new unknown term and, therefore, it requires of extra equations to solve the system. These new equations that account for the turbulence part of the system are called RANS Turbulence Models. The Boussinesq hypothesis states that the Reynolds stress tensor is proportional to the mean strain rate tensor, multiplied by a constant, which is called turbulent eddy viscosity, μ_t. In the case of incompressible flow:

$$R_{ij} = \mu_t\left(\frac{\partial\overline{u_i}}{\partial x_j} + \frac{\partial\overline{u_j}}{\partial x_i}\right) - \frac{2}{3}\rho k\delta_{ij} \tag{2.11}$$

Therefore, the objective of these methods is to derive said turbulent viscosity. Some of the most employed methods are:

- **Spalart-Allmaras** (SA). The SA model uses a transport equation (Equation 2.12) to solve for a modified kinematic eddy viscosity, $\tilde{\nu}$, as a function of the kinematic eddy viscosity $\nu_t = \mu_t/\rho$.

  $$\frac{\partial\tilde{\nu}}{\partial t} + \overline{u}_j\frac{\partial\tilde{\nu}}{\partial x_j} = \frac{1}{\sigma}\left[\frac{\partial}{\partial x_j}\left((\nu+\tilde{\nu})\frac{\partial\tilde{\nu}}{\partial x_j}\right) + C_{b2}\frac{\partial\tilde{\nu}}{\partial x_j}\frac{\partial\tilde{\nu}}{\partial x_j}\right] + P_{\tilde{\nu}} + D_{\tilde{\nu}} \tag{2.12}$$

  In the equation, $P_{\tilde{\nu}}$ and $D_{\tilde{\nu}}$ refers to the production and destruction terms of $\tilde{\nu}$, respectively. The turbulent eddy viscosity is computed from Equation 2.13, where $f_{\nu 1}$ is the viscous damping function.

  $$\mu_t = \rho\tilde{\nu}f_{\nu 1} \tag{2.13}$$

  The model was specifically derived for use in aerodynamic applications involving wall-bounded systems as well as in turbomachinery applications [19]. It presents some advantages such as the dimensionality reduction, as it employs a single turbulent equation, which decreases the complexity of the problem and the overall simulation time.

- **K-Epsilon** ($k - \varepsilon$). The standard $k - \varepsilon$ model focuses on the mechanisms that affect the turbulent kinetic energy. It uses two transport equations, one for the turbulent kinetic energy, k (Equation 2.14) and one for the turbulent dissipation rate, ε (Equation 2.15).

$$\frac{\partial(\rho k)}{\partial t} + \frac{\partial(\rho \overline{u}_j k)}{\partial x_j} = \frac{\partial}{\partial x_j}\left[\left(\mu + \frac{\mu_t}{\sigma_k}\right)\frac{\partial k}{\partial x_j}\right] + 2\mu_t S_{ij} S_{ij} - \rho\varepsilon \tag{2.14}$$

$$\frac{\partial(\rho \varepsilon)}{\partial t} + \frac{\partial(\rho \overline{u}_j \varepsilon)}{\partial x_j} = \frac{\partial}{\partial x_j}\left[\left(\mu + \frac{\mu_t}{\sigma_\varepsilon}\right)\frac{\partial \varepsilon}{\partial x_j}\right] + C_{\varepsilon 1}\frac{\varepsilon}{k} 2\mu_t S_{ij} S_{ij} - C_{\varepsilon 2}\rho\frac{\varepsilon^2}{k} \tag{2.15}$$

and the turbulent eddy viscosity is computed from

$$\mu_t = \rho C_\mu \frac{k^2}{\varepsilon} \tag{2.16}$$

The equations include five adjustable constants that have been obtained empirically for a wide range of turbulent flows [20]:

$$C_\mu = 0.09; \quad \sigma_k = 1; \quad \sigma_\varepsilon = 1.3; \quad C_{\varepsilon 1} = 1.44; \quad C_{\varepsilon 2} = 1.92 \tag{2.17}$$

The model has been shown to be useful for free-shear layer flows with small adverse pressure gradients and confined flows where the turbulence is predominantly homogeneous and the flow is well-developed, and an inappropriate choice for problems such as inlets and compressors.

- **SST K-Omega** (*SST* $k - \omega$). The $k - \omega$ is another two equation model that solves the turbulent kinetic energy, k (Equation 2.18) and the specific dissipation rate, ω, to determine the turbulent eddy viscosity (Equation 2.19). The model is particularly effective in capturing the behavior of turbulent flows near walls without the need for complex wall functions. This makes it well-suited for boundary layer flows, especially those with adverse pressure gradients and separation. The *Shear Stress Transport* (SST) formulation combines the $k - \omega$ formulation in the inner parts of the boundary layer, and the $k - \varepsilon$ behaviour in the free-stream [21].

$$\frac{\partial(\rho k)}{\partial t} + \frac{\partial(\rho \overline{u}_j k)}{\partial x_j} = \frac{\partial}{\partial x_j}\left[(\mu + \sigma_k \mu_t)\frac{\partial k}{\partial x_j}\right] + 2\mu_t S_{ij} S_{ij} - \beta^* \rho\omega k \tag{2.18}$$

$$\frac{\partial(\rho \omega)}{\partial t} + \frac{\partial(\rho \overline{u}_j \omega)}{\partial x_j} = \frac{\partial}{\partial x_j}\left[(\mu + \sigma_\omega \mu_t)\frac{\partial \omega}{\partial x_j}\right] + 2\mu_t S_{ij} S_{ij}\frac{\gamma}{\nu_t} - \beta\rho\omega^2 + P_\omega \tag{2.19}$$

The equations include several parameters and relations of μ_t which is computed as a function of k and ω. The model is the most widely accepted industry standard turbulence model, as it provides more reliable results in external aerodynamic applications, better capture of the transition from laminar to turbulent flow, and it can handle complex flow phenomena, including separation, recirculation, and reattachment.

2.4 Boundary Layer

The concept of boundary layer was first introduced by Prandtl in 1904. The boundary layer is a thin region of flow adjacent to a surface, where the flow slows down by the influence of significant shear stress between the fluid and the solid surface by the no-slip condition [22]. At the boundary layer, the flow velocity increases in the y direction from zero at the wall to the free-stream velocity. As a consequence of this, the boundary layer thickness, δ, is defined as the height above the wall where $u = 0.99U_\infty$. The thickness of the boundary layer increases monotonically with the distance from the leading edge, x, therefore, $\delta = \delta(x)$. Within the boundary layer the flow can be laminar or turbulent, leading to two different types of boundary layer, defined by the Reynolds number.

At low Re, the boundary layer remains laminar, and the fluid particles move in smooth, orderly layers, in a parabolic velocity profile. After a critical local Reynolds, $Re_{x,crit}$, the boundary layer transitions into turbulent. The velocity profile becomes fuller and flatter compared to the laminar profile, with a steep gradient near the wall. This is represented on Figure 2.2. Due to their higher momentum transfer and mixing near the wall, turbulent boundary layers can better resist the flow separation, and the separation point occurs further downstream compared to laminar flow [23].

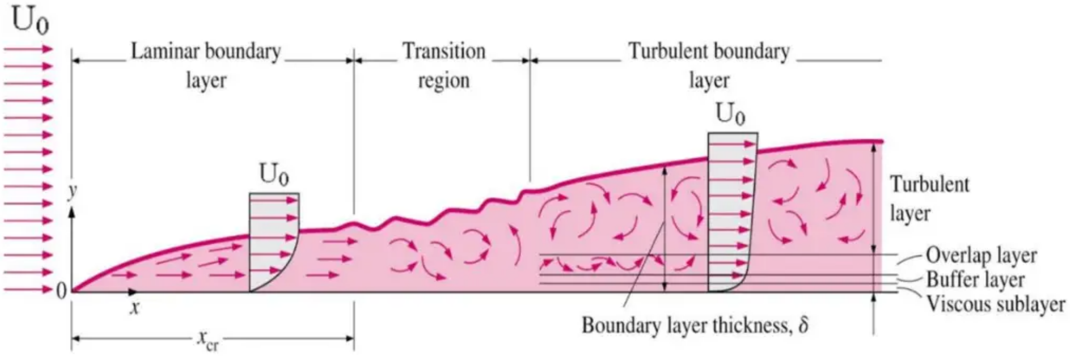

Figure 2.2: Boundary layer over a flat plate. Image taken from [24].

Within the turbulent boundary layer, the influence of viscosity is confined to a very thin region right next to the wall. This region is known as the *viscous sublayer*. Here, the flow is nearly laminar, and the velocity profile is linear. Beyond the viscous sublayer is the *buffer layer*, a transition zone where both viscous and turbulent effects are significant. The velocity profile starts to deviate from linearity, and turbulence starts to become more pronounced but is not fully developed. Further from the wall lies the *logarithmic layer* or *log-law region*. This region, is dominated by turbulent shear stresses, turbulence is fully developed, and the velocity profile follows the logarithmic relationship (Equation 2.23). Finally, the *outer layer*, extends from the edge of the logarithmic layer to the boundary layer's outer edge. In this region, the influence of the wall diminishes, and the velocity profile is influenced by the overall pressure gradient and free-stream conditions.

The consequence of the velocity gradient at the wall is the generation of shear stress at the wall, τ_w, where the index w denotes the value at the wall ($y = 0$).

$$\tau_w = \mu \left(\frac{\partial u}{\partial y} \right)_w \tag{2.20}$$

Inside the viscous sublayer the velocity profile is linear, and the gradient can be considered constant. Therefore,

$$\tau_w = \mu \frac{U}{y} = \rho\nu \frac{U}{y} \tag{2.21}$$

From here, the wall shear stress may be re-written in units of velocity as the friction velocity, $u_\tau = \sqrt{\tau_w/\rho}$. Substituting this result into the previous equation, two nondimensional parameters are obtained: the dimensionless velocity (parallel to the wall), U^+, and the wall coordinate, y^+.

$$U^+ = \frac{U}{u_\tau} = y^+ = \frac{y u_\tau}{\nu} \tag{2.22}$$

Equation 2.22 is known as the Law of the wall. In the viscous sublayer, the equation is consistent with the experimental results in the range $0 \leq y^+ \leq 5$. Beyond, the buffer layer spans between $5 \leq y^+ \leq 30$. Finally, the logarithmic layer extends from $y+ = 30$ to $y/\delta \approx 0.1 - 0.3$. As previously stated, in the logarithmic layer the behaviour of the velocity is expressed by a logarithmic law given by

$$U^+ = \frac{1}{\kappa} \ln y^+ + C^+ \tag{2.23}$$

where κ is the von Kármán constant and C^+ is an empirical constant.

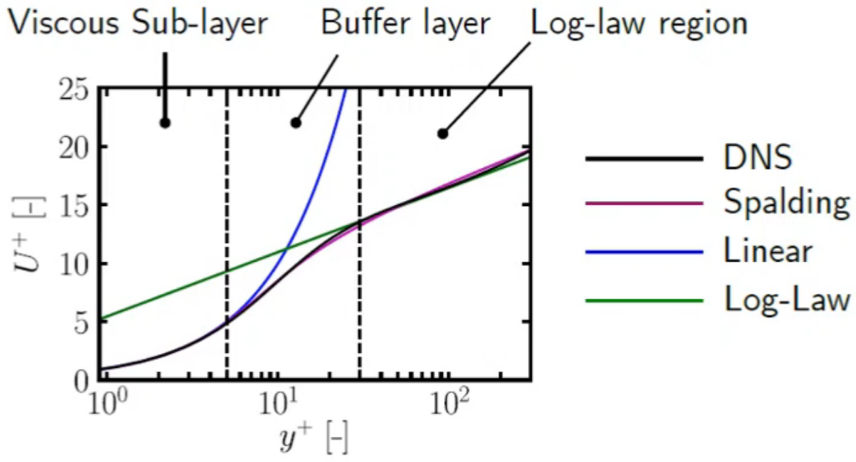

Figure 2.3: Non-dimensional velocity profile in a boundary layer. Image taken from [25].

In CFD simulations an accurate modeling of the boundary layer is crucial as it determines τ_w, for calculating frictional drag on surfaces and for determining the forces acting on structures. In addition, it is essential for predicting flow separation and reattachment, which can significantly affect the aerodynamic performance of bodies. Simplified models (such as Spalding wall function) are often used to approximate the behavior of the boundary layer, especially in high Reynolds number flows, to reduce computational cost while maintaining accuracy. The most common approach involves mesh refinement near the wall to resolve the steep gradients in the boundary layer.

2.5 Numerical approach

Discretization is a fundamental step in CFD that involves converting the system of continuous transport equations into discrete algebraic equations that can be solved numerically. In order to convert the system, the domain is discretized into a finite number of elements and the resulting equations are resolved using different mathematical schemes and algorithms. All the transport equations can be expressed in a generic form, allowing a systematic approach for computer simulation.

$$\underbrace{\frac{\partial \rho\phi}{\partial t}}_{Transient\ term} + \underbrace{\nabla\cdot(\rho\boldsymbol{u}\phi)}_{Convection\ term} = \underbrace{\nabla\cdot(\Gamma\nabla\phi)}_{Diffusion\ term} + \underbrace{S_\phi}_{Source\ term} \tag{2.24}$$

In the equation, the depending variable is denoted by ϕ; the transient term accounts for the accumulation of ϕ in the control volume; the convection term, for the transport of ϕ in presence of a velocity field; the diffusion term, for the transport of ϕ due to its gradients, with Γ being the diffusivity; and the source term that accounts for any production or destruction of ϕ.

Several methods can be used to discretize the transport equations, with the most common ones being the *Finite Element Method* (FEM), *Finite Differences Method* (FDM), or *Finite Volumes Method* (FVM). FVM is the method most used in the majority of CFD software. It integrates the governing equation over small controll volumes (or cells), and applies the divergence theorem to convert the volume integrals into surface integrals. These terms are then evaluated as fluxes at the surfaces of each finite volume, resulting in

$$\frac{\partial}{\partial t}(\rho\phi V) + \sum_f(\rho\phi\boldsymbol{u}\cdot\boldsymbol{A})_f = \sum_f(\Gamma\nabla\phi\cdot\boldsymbol{A})_f + S_\phi V \tag{2.25}$$

where the subscript f denotes quantities evaluated at the faces of the control volumes, V is the control volume and $\boldsymbol{A}$ is the face area vector.

2.5.1 Spacial Discretization

The spatial domain and fluxes across the faces at each control volume are discretized. Some of the most common schemes include:

- Central Differencing Scheme. 2nd order method that uses the average of values from adjacent cells to approximate the value at the face of a control volume. It provides higher accuracy for smooth solutions, but may introduce numerical diffusion, especially in advection-dominated flows.

- Upwind Differencing Scheme. 1st order method that uses the value from the upstream cell, based on the flow direction, to approximate the value at the face. Upwind scheme provides a stable solution for advection-dominated flows. However, 1st order methods are less accurate due to higher numerical diffusion.

- Hybrid Differencing Schemes. Combine central and upwind differencing to balance accuracy and stability.

- Higher-Order Schemes such as QUICK (*Quadratic Upstream Interpolation for Convective Kinematics*) or MUSCL (*Monotone Upstream-Centered Schemes for Conservation Laws*).

2.5.2 Temporal Discretization

For unsteady problems, time derivatives also need to be discretized. The stability requirements of time discretization schemes can be determined using the Courant-Friedrichs-Lewy (CFL) condition [26]. It is expressed by the Courant number, which represents the ratio of the time step to the grid spacing. The CFL must be kept below a certain threshold, typically 1, to ensure the stability of the solution and prevent the growth of numerical errors.

$$CFL = \frac{U\Delta t}{\Delta x} \leq CFL_{max} \tag{2.26}$$

In CFD simulations, the Courant number essentially measures how far information travels through a computational grid cell within a single time step. When the Courant number is greater than one, information spans more than one grid cell per time step, which can lead to inaccuracies and possibly nonphysical results or divergence, depending on the chosen integration scheme.

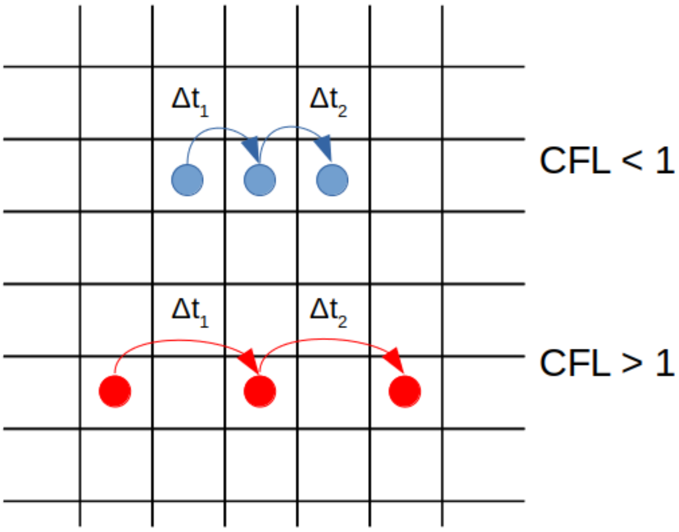

Figure 2.4: Visualisation of the Courant number and the CFL condition on a computational grid. Image taken from [27].

Some of the most common methods employed are explicit, implicit and semi-implicit methods:

- Explicit Methods compute the new time step directly from known information at the current time step. Explicit methods are conditionally stable, constrained by the CFL condition. Some examples are Forward Euler or Runge-Kutta methods.
- Implicit Methods involve solving a system of equations at each time step, offering better stability properties, especially for stiff problems. Implicit methods, such as Backward Euler, are unconditionally stable, meaning that they can handle large CFL numbers without causing instability.
- Semi-Implicit Methods combine features of both explicit and implicit methods to balance stability and computational efficiency.

2.5.3 Numerical Algorithms

Transport equations are thus solved numerically. The choice of solver is fundamental and influences the computational efficiency, stability, and accuracy of the simulation.

Coupled solvers solve all the equations simultaneously, accounting for the interactions between different variables at each iteration step, leading to potentially better stability and faster convergence. They are often more robust and particularly advantageous for transient problems, compressible flows, and flows with strong interactions between different physical phenomena.

Segregated solvers solve the transport equations sequentially. This means that the transport equations are solved one after the other within each iteration. Typically, the momentum equations are solved first, followed by the pressure correction equation, e.g. using SIMPLE or PISO algorithms.

- **SIMPLE**. The *Semi-Implicit Method for Pressure-Linked Equations* algorithm is an iterative method used to solve the continuity and momentum equations for incompressible flows.
- **PISO**. The *Pressure-Implicit with Splitting of Operators* algorithm is an extension of the SIMPLE algorithm that aims to improve convergence for transient problems. It is particularly useful for problems where pressure-velocity coupling is strong.

Segregated solvers can suffer from slow convergence, particularly for problems with strong coupling between variables. Also, they may require under-relaxation factors to ensure stability, which can further slow down convergence.

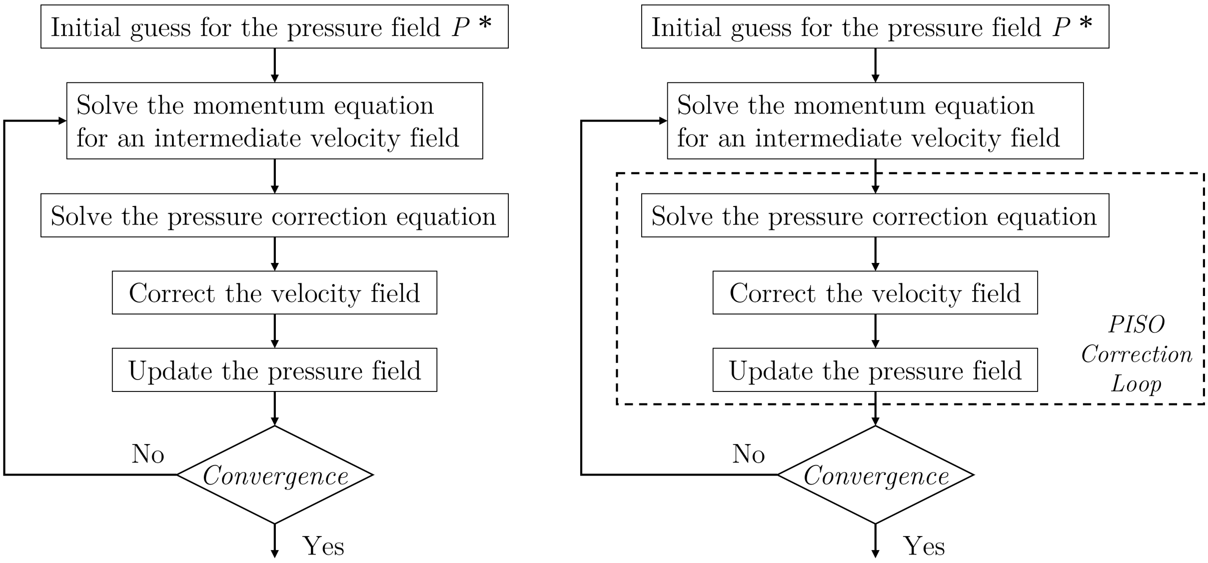

Figure 2.5: Algorithm of the segregated solvers. SIMPLE (left) and PISO (right).

Chapter 3

Fundamentals of Rotor Aerodynamics

3.1 Introduction

The understanding of rotor aerodynamics is a critical field of study in the design and analysis of rotary-wing aircraft, such as helicopters and drones. Understanding the aerodynamic behaviour of rotors is essential for optimizing their performance. Over time, rotor aerodynamics has been approached using different analytical models, such as momentum theory and blade element theory, which have evolved to become more sophisticated and accurate. The study of rotor aerodynamics has also been aided by advances in computational fluid dynamics and experimental techniques. By studying rotor aerodynamics, the complex flow phenomena that occur in and around rotors can be understand, and use this knowledge to develop more efficient and effective rotor systems.

Unlike fixed-wing aircraft, which generate lift through the flow of air over a fixed-wing surface, rotary-wing aircraft generate lift by creating a downward flow of air over a rotating-wing surface. This creates a complex flow field that is highly unsteady and three-dimensional, with significant variations in velocity and pressure across the rotor disc. Additionally, rotary-wing aircraft are highly manoeuvrable and capable of vertical takeoff and landing, which requires a different set of aerodynamic principles and design considerations. This chapter provides an overview of the fundamental concepts and theories that underlie rotors aerodynamics.

3.2 Momentum Theory

Momentum Theory provides a simplified approach to analysing the performance of a rotor system. It allows for calculating the rotor thrust and power, by considering the rotor as an actuator disc. It assumes that the flow through the rotor is one-dimensional, quasi-steady, incompressible and inviscid.

A control volume surrounding the rotor and its wake is considered as represented in Figure 3.1. Three different planes can be considered: 0 being the plane far upstream of the disc; 1 and 2, the planes above and below the rotor disc, respectively; and ∞ denoting the far wake downstream of the rotor. Assuming that the velocity generated by the rotor is v_i, and that the relative velocity far upstream relative to the rotor is V_c, the velocity at the plane of the rotor is, therefore, $V_c + v_i$, and the slipstream velocity $V_c + w$.

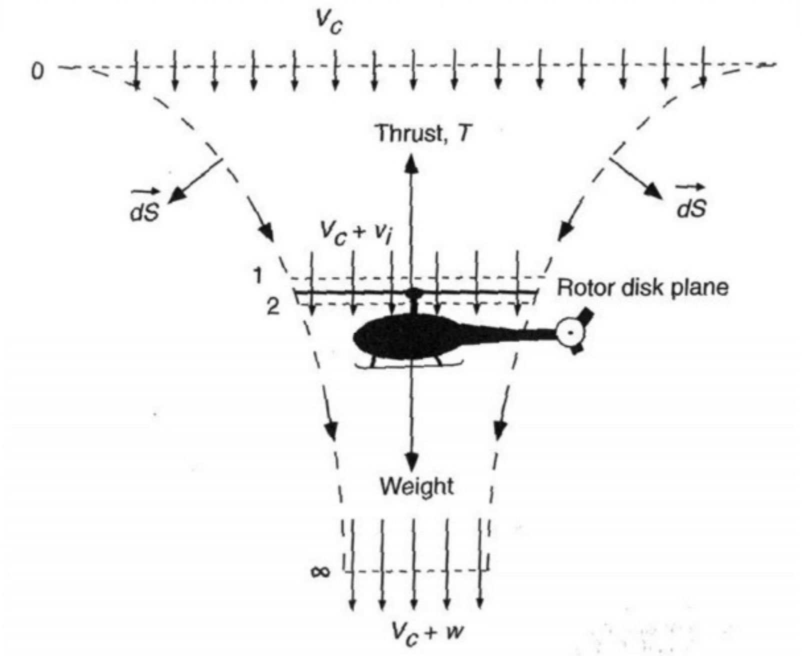

Figure 3.1: Control volume and variables involved in Momentum Theory. Image taken from [28].

The physical principles governing the problem are again the conservation of mass, momentum and energy. Thus, conservative equations are applied to the finite control volume. By the conservation of mass, the mass flow rate must be constant inside the boundaries, so

$$\dot{m} = \iint_{\infty} \rho \vec{V} \cdot d\vec{S} = \iint_{2} \rho \vec{V} \cdot d\vec{S} \tag{3.1}$$

where $d\vec{S}$ is the normal surface vector pointing outward from the control volume. Substituting values, the equation results in

$$\dot{m} = \rho A_{\infty}(V_c + w) = \rho A(V_c + v_i) \tag{3.2}$$

The conservation of momentum gives

$$T = \iint_{\infty} \rho(\vec{V} \cdot d\vec{S})\vec{V} - \iint_{0} \rho(\vec{V} \cdot d\vec{S})\vec{V} \tag{3.3}$$

Therefore, in this case

$$T = \dot{m}(V_c + w) - \dot{m}V_c = \dot{m}w \tag{3.4}$$

Finally, from the energy conservation, the work done on the rotor must be equal to the energy gained by the fluid per unit of time, resulting in

$$T(V_c + v_i) = \iint_{\infty} \frac{1}{2}\rho(\vec{V} \cdot d\vec{S})\vec{V}^2 - \iint_{0} \frac{1}{2}\rho(\vec{V} \cdot d\vec{S})\vec{V}^2 \tag{3.5}$$

then,

$$T(V_c + v_i) = \frac{1}{2}\dot{m}(V_c + w)^2 - \frac{1}{2}\dot{m}V_c^2 = \frac{1}{2}\dot{m}w(2V_c + w) \tag{3.6}$$

From this result and combining it with Equation 3.4, it is obtained that $w = 2v_i$. Thus, the expressions for both the thrust and power are as follows:

$$T = 2\rho A v_i(V_c + v_i) \tag{3.7}$$

$$P = T(V_c + v_i) = 2\rho A v_i(V_c + v_i)^2 \tag{3.8}$$

3.3 Blade Element Theory

Blade element theory (BET) is a more advanced method for analysing rotor aerodynamics, which takes into account the local variation of aerodynamic forces along the rotor blade. This approach divides the rotor blade into small elements and calculates the aerodynamic forces and moments acting on each element. These are then integrated along the length of the blade to obtain the overall performance characteristics of the rotor. BET allows for a more accurate prediction of rotor performance, as it accounts for the effects of blade geometry, twist, and airfoil characteristics on the aerodynamic forces [29]. Figure 3.2 shows a sketch of a blade element at a radial distance y, as well as the reference system utilised and the decomposition of velocities and forces.

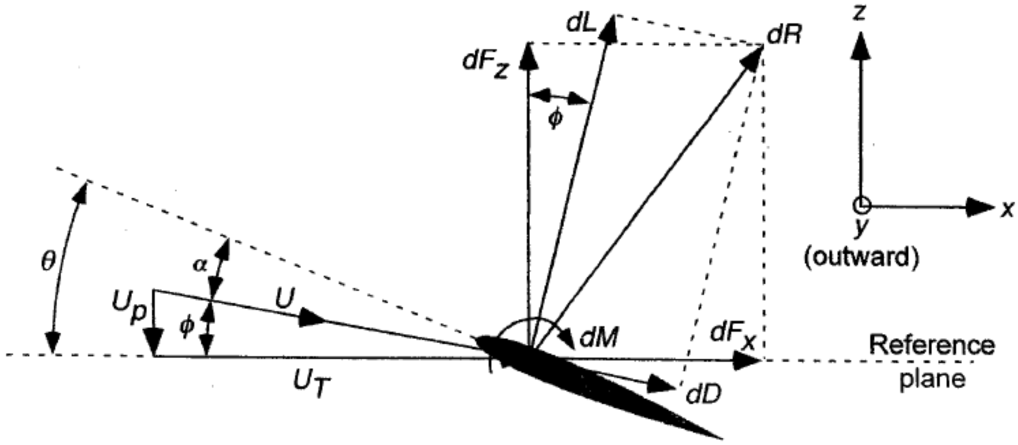

Figure 3.2: Velocities and aerodynamic forces representation in BET. Image taken from [28].

The velocity at any blade element has an out-of-plane component $U_P = V_c + v_i$ normal to the rotor, and a tangential component $U_T = \Omega y$ parallel to the rotor with Ω being the angular velocity of blade rotation. The resultant velocity is, therefore,

$$U = \sqrt{U_T^2 + U_P^2} \tag{3.9}$$

The induced angle of attack at the blade, considering small angles, is expressed as

$$\phi_i = \arctan\left(\frac{U_P}{U_T}\right) \approx \frac{U_P}{U_T} = \frac{V_c + v_i}{\Omega y} \tag{3.10}$$

thus, for a pitch angle θ, the aerodynamic angle of attack is

$$\alpha = \theta - \phi_i = \theta - \frac{V_c + v_i}{\Omega y} \tag{3.11}$$

The differential aerodynamic forces per unit of span are

$$dL = \frac{1}{2}\rho U^2 c C_l dy \tag{3.12}$$

$$dD = \frac{1}{2}\rho U^2 c C_d dy \tag{3.13}$$

where C_l and C_d are the aerodynamic lift and drag coefficients, respectively.

From Figure 3.2, the forces acting perpendicular and parallel to the rotor disc can be solved, resulting in the following equations for thrust, torque and power of the rotor:

$$dT = N_b(dL\cos\phi_i - dD\sin\phi_i) \tag{3.14}$$

$$dQ = N_b(dL\sin\phi_i + dD\cos\phi_i)y \tag{3.15}$$

$$dP = N_b(dL\sin\phi_i + dD\cos\phi_i)\Omega y \tag{3.16}$$

with N_b the number of blades in the rotor. Considering a small induced angle ϕ_i so that $\sin\phi_i \approx \phi_i$ and $\cos\phi_i \approx 1$, and that the contribution of $dD\phi_i$ is negligible, the previous equations simplify to

$$dT = N_b dL \tag{3.17}$$

$$dQ = N_b(dL\phi_i + dD)y \tag{3.18}$$

$$dP = N_b(dL\phi_i + dD)\Omega y \tag{3.19}$$

From here, it is convenient to express the quantities in non-dimensional form. The coefficients of are expressed as

$$dC_T = \frac{dT}{\rho A(\Omega R)^2} \qquad dC_Q = \frac{dQ}{\rho A(\Omega R)^2 R} \qquad dC_P = \frac{dP}{\rho A(\Omega R)^3} \tag{3.20}$$

The inflow ratio is defined as the ratio between the normal velocity and the tangential velocity at the blade tip. It can be written as

$$\lambda = \frac{V_c + v_i}{\Omega R} = \frac{V_c + v_i}{\Omega y}\left(\frac{y}{R}\right) = \phi_i r \tag{3.21}$$

with r being the non-dimensional radial coordinate. Another important parameter is the rotor solidity σ. It is defined as the ratio of the total blade area to the total rotor disc area, which for a constant chord blade is formulated as

$$\sigma = \frac{N_b c}{\pi R} \tag{3.22}$$

Therefore, the increment in thrust coefficient is

$$dC_T = \frac{N_b dL}{\rho A(\Omega R)^2} = \frac{1}{2}\left(\frac{N_b c}{\pi R}\right) C_l r^2 dr = \frac{1}{2}\sigma C_l r^2 dr \tag{3.23}$$

Increasing the solidity of a rotor blade is known to improve its lift and thrust capabilities. However, this improvement comes at the cost of increased drag and downwash, both of which can negatively impact the rotor's performance, efficiency, and noise characteristics. As such, balancing the trade-offs between these factors is an important consideration when designing rotors for various applications.

3.4 Blade Element Momentum Theory

The blade element momentum theory (BEMT) combines the principles from both previous approaches. BET requires to know the inflow distribution beforehand or computing it by iterative methods. Here, BEMT allows the estimation of the inflow distribution along the blade by considering the fluid-rotor system as several annuli of the rotor disc which do not interact with each other, analysed using Momentum theory and the differential analysis of Blade Element theory.

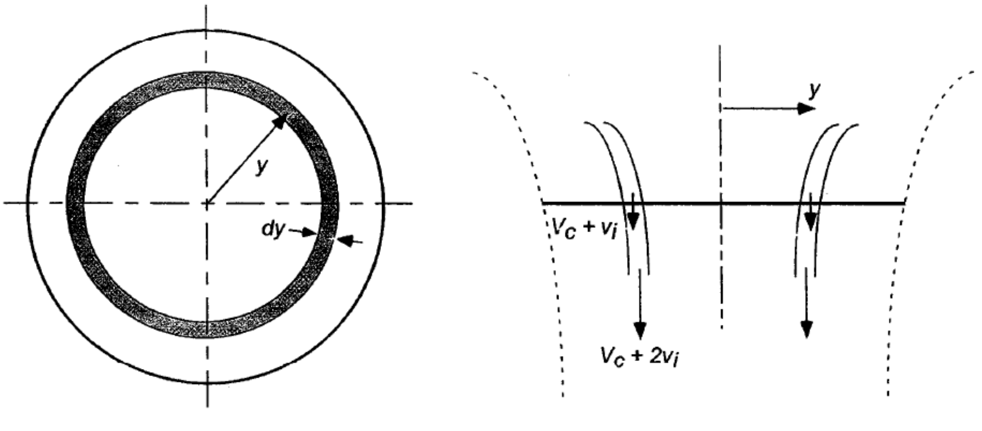

Figure 3.3: Annulus of rotor disc used for local momentum analysis. Top view (right), cross-sectional view (left). Image taken from [28].

The conservation equations are applied to an annulus of the rotor disc, located at distance y, and width dy as shown in Figure 3.3. The incremental thrust can be calculated by applying momentum theory and results in

$$dT = 2\rho(V_c + v_i)v_i dA = 4\pi\rho(V_c + v_i)v_i y dy \tag{3.24}$$

then, the incremental thrust coefficient expressed in terms of non-dimensional quantities can be written as

$$dC_T = 4\lambda\lambda_i r dr \tag{3.25}$$

with $\lambda_i = v_i/(\Omega R)$ and $\lambda_c = V_c/(\Omega R)$, so that $\lambda_i = \lambda - \lambda_c$. Now by equating the expression obtained with Equation 3.25 and solving for the inflow ratio λ, the radial inflow equation is obtained as

$$\lambda(r, \lambda_c) = \sqrt{\left(\frac{\sigma C l_\alpha}{16} - \frac{\lambda_c}{2}\right)^2 + \frac{\sigma C l_\alpha}{8}\theta r} - \left(\frac{\sigma C l_\alpha}{16} - \frac{\lambda_c}{2}\right) \tag{3.26}$$

Equation 3.26 allows for the solution of the induced velocity as a function of the radius by knowing the geometry of the blades, the airfoils and the velocities. The thrust and power of the rotor can be determined by integrating incremental values across the blade's span. This approach can provide valuable insights into the performance of the rotor, however, it is only reliable far from the blade tips.

3.4.1 Prandtl's Tip-Loss Function

It is possible to account for the lift loss near the tips resulting from the induced effects associated with a finite number of blades through Prandtl's Tip-Loss Function. Here, the curved helical vortex sheets of the rotor wake are substituted by a series of two-dimensional vortex sheets. The results are expressed in terms of Prandtl's tip loss factor, F, being

$$F = \left(\frac{2}{\pi}\right) \arccos(\exp(-f)) \tag{3.27}$$

with $f = \frac{N_b}{2}\left(\frac{1-r}{r\phi_i}\right)$ and $\phi_i = \lambda_i / r$.

F function increases the induced velocity near the tips, thus reducing the lift generated in that area. Figure 3.4 plots the tip loss function versus the non-dimensional radial coordinate for different values of ϕ_i and N_b. It is observed that F always has a lower value for fewer blades. This is because in the limit case $N_b \to \infty$ and $F \to 1$, the rotor approximates to a rotor disc, and the circulation is distributed uniformly. Besides, as the blade tip is approached, the value of F is reduced due to the effects of the vortex wake.

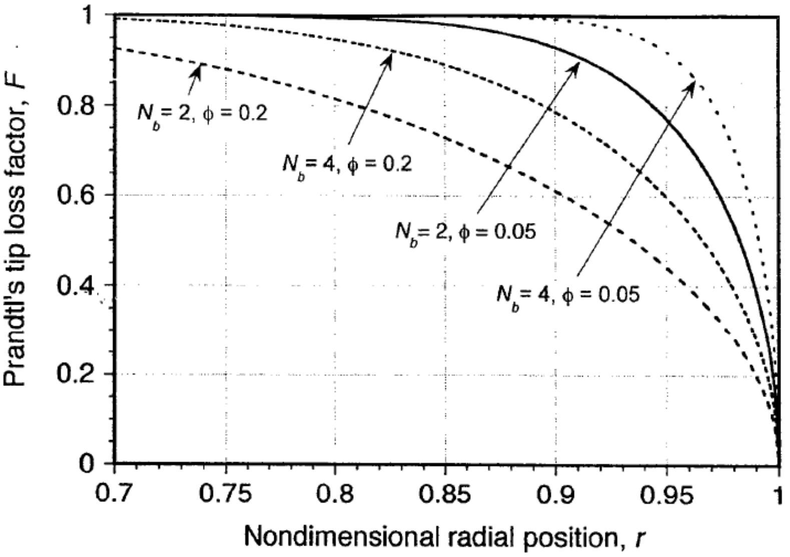

Figure 3.4: Prandtl's tip loss factor versus radial coordinate. Image taken from [28].

Now, Equation 3.25 can be modified by introducing the tip loss factor, resulting in

$$dC_T = 4F\lambda\lambda_i r dr \tag{3.28}$$

which by merging it with the result from BET, it is possible to obtain an expression to solve for the inflow ratio. Considering hovering flight ($V_c = 0$),

$$\lambda_i(r) = \frac{\sigma Cl_\alpha}{16F}\left(\sqrt{1+\frac{32F}{\sigma Cl_\alpha}\theta r} - 1\right) \tag{3.29}$$

This leads to an equation involving λ and F which is solved iteratively by first guessing a value of $F = 1$.

3.5 Aerodynamic coefficients of propellers and rotors

Similar to airfoils and wings, the performance of propellers can be described by dimensionless coefficients. Whereas an airfoil can be characterized by relationships between the angle of attack, lift coefficient, and drag coefficient, a propeller can be described in terms of the advance ratio, J, which expresses the distance travelled with one turn of the propeller, thrust coefficient, C_T, and power coefficient, C_P. The efficiency of a propeller, η, which is analogous to the lift-to-drag ratio of a wing, can be calculated from these three coefficients. These coefficients are useful for comparing propellers of differing diameters that have been tested under various operating conditions [30]. Said coefficients are expressed as

$$J = \frac{V}{nD} \tag{3.30}$$

$$C_T = \frac{T}{\rho n^2 D^4} \tag{3.31}$$

$$C_P = \frac{P}{\rho n^3 D^5} \tag{3.32}$$

Sometimes it is interesting to express the torque coefficient, $C_Q = C_P/(2\pi)$ which represents the torque required to counteract the resistance exerted by the fluid on the blade rotation. The efficiency is defined as the ratio between the product of the thrust generated by the propeller and the advance speed, and the power of the propeller.

$$\eta = \frac{TV}{P} \tag{3.33}$$

Therefore, it can be expressed by employing the coefficients above defined, resulting in

$$\eta = J\frac{C_T}{C_P} \tag{3.34}$$

In addition to these dimensionless coefficients, two other parameters defining the aerodynamic behaviour of the propeller are involved in the analysis of its performance. These are the Mach number (Equation 3.35), which relates the rotor's speed with the speed of sound, and the Reynolds number (Equation 3.36), which is the ratio between the inertial and viscous forces.

$$M = \frac{nD}{a} \tag{3.35}$$

$$Re = \frac{\rho n D^2}{\mu} \tag{3.36}$$

Table 3.1 shows the variables of interest in the performance analysis of propellers. Therefore, the performance of a propeller can be expressed by performance maps, representing main performance coefficients as a function of the flying conditions, i.e. $C_T = C_T(J, M, Re)$ and $C_P = C_P(J, M, Re)$. It can be demonstrated that the Reynolds number does not affect the propeller's performance.

Variable	**Symbol**	**Units**
Diameter of the propeller	D	m
Fluid's relative velocity	V	m/s
Fluid's density	ρ	kg/m^3
Fluid's dynamic viscosity	μ	Pa · s
Rotation speed	n	s^{-1}
Speed of sound	a	m/s

Table 3.1: Variables involved in propeller aerodynamic analyses.

Chapter 4

Methodology

4.1 Introduction

The methodology of a CFD study involves several key steps to ensure accurate and reliable simulation results. The diagram in Figure 4.1 represents the flow chart followed along the development of the CFD study, and involves the following major steps:

- **Geometry preparation**. The initial step involves importing and preparing the geometric model. This includes cleaning up the geometry to ensure it is suitable for meshing and simulation.
- **Meshing strategy**. Creating a high-quality computational mesh is critical for capturing the aerodynamic phenomena accurately. This involves generating surface and volume meshes with appropriate refinements in critical regions, and a mesh independence study to evaluate the accuracy and computational cost of the mesh employed.
- **Physics Setup**. Defining the physical models and boundary conditions relevant to the problem. This includes setting up the fluid properties, turbulence models, and any other physical phenomena being studied.
- **Solver Configuration**. This step involves configuring the solver settings, including convergence criteria, time step selection for unsteady simulations, and numerical schemes to ensure stable and accurate solutions.
- **Post-Processing**. Finally, the simulation results are analysed to extract meaningful insights. This involves visualizing flow fields, calculating performance metrics, and validating the results against experimental or theoretical data.

The detailed discussion in the subsequent sections will provide a comprehensive understanding of each step in the CFD process, ensuring that the study is reproducible and scientifically rigorous.

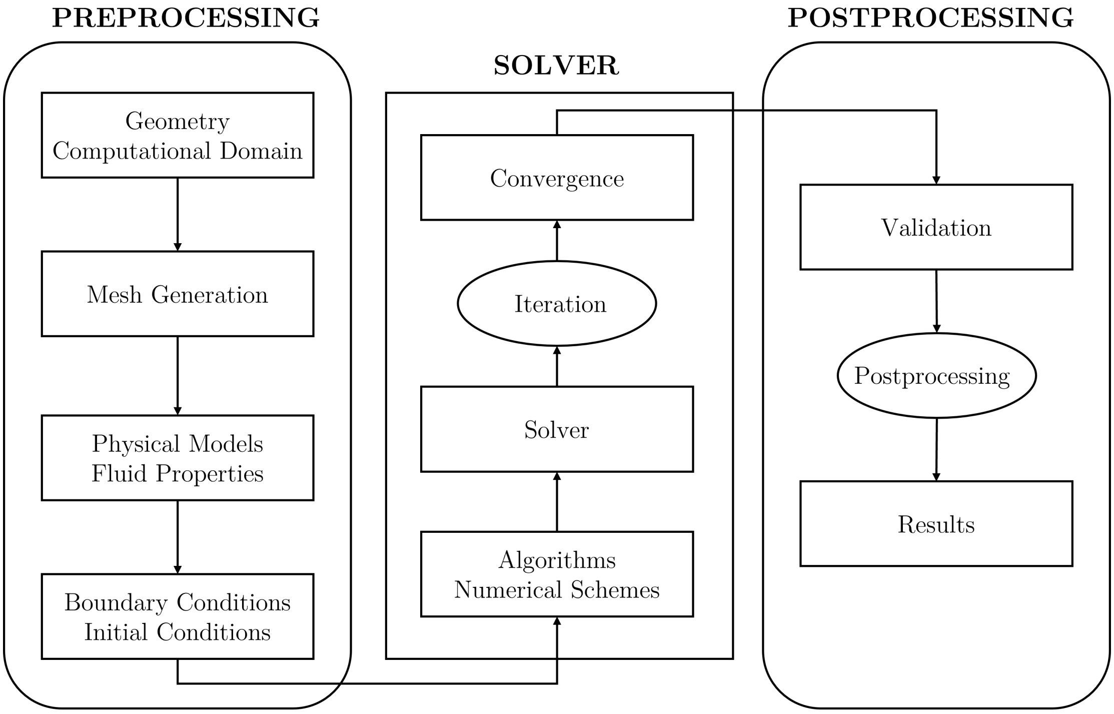

Figure 4.1: CFD methodology flow chart.

4.2 STAR-CCM+ Simulation

4.2.1 Geometry and Computational Domain

The geometry utilised in the simulations consists of an experimental flat plate propeller, shown in Figure 4.2. It is made up of two flat rectangular plate blades of aspect ratio equal to $AR = 8$, whose main dimensions are: chord ($c = 0.05$ m), blade span ($s = 0.4$ m), and thickness ($h = 1.57$ mm). The rotor hub consists of a cylindrical shape with diameter $D_{hub} = 0.15$ m, totalling a blade diameter of $D = 0.95$ m.

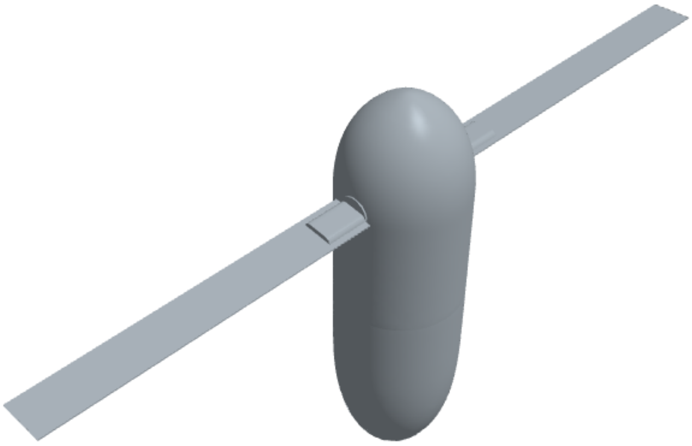

Figure 4.2: Geometry model of the propeller employed in the simulations.

The computational domain refers to the physical volume over which the fluid flow is simulated and the fluid equations are solved. The domain size is constructed in a manner such that the boundary conditions do not influence the solution obtained over the propeller surface. The fluid domain consists of an external cylinder (Figure 4.3) and a cylindrical rotating region that surrounds the propeller in which the rotatory motion is applied (Figure 4.4). The dimensions of both regions are shown in Table 4.1.

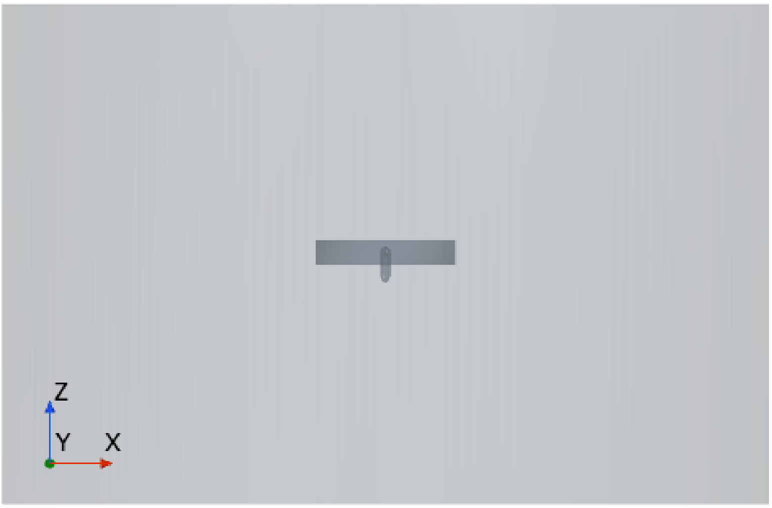

Figure 4.3: Computational domain (front view).

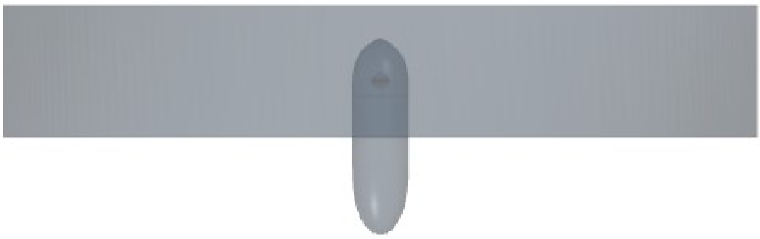

Figure 4.4: Rotating region.

Dimension	**Symbol**	**Value** [m]
Fluid domain's Diameter	D_d	11
Fluid domain's Height	H_d	7.18
Rotating region's Diameter	D_r	2
Rotating region's Height	H_r	0.35

Table 4.1: Main dimensions of the computational domain.

4.2.2 Meshing strategy

The accuracy and reliability of CFD simulations heavily depend on the quality of the computational mesh. In this study, a carefully designed meshing strategy was developed to ensure the accurate capture of aerodynamic phenomena around the propeller, ensuring adequate resolution in critical regions. The main characteristic of the volume mesh are listed as follows.

- **Mesh Type**. An unstructured mesh with polyhedral elements was chosen for its flexibility in handling complex geometries and ability to provide high-quality elements, while reducing the number of total elements.
- **Growth Rate**. A growth rate of 1.05 is defined for both surfaces and volumes to ensure a smooth transition between elements.
- **Refinement Zones**. Specific regions of interest, such as the boundary layers around the propeller blades and the wake region behind the propeller, were refined to capture important flow features.

Zone	**Control type**	**Relative to Base Size** [%]
Wake	Volume	16
Rotating Region	Volume	5
Hub and clamping	Surface	2
Blades	Surface	1
Blade edges	Surface	0.125

Table 4.2: Refinement zones values.

- **Boundary Layer**. As explained in section 2.4, for a correct calculation of forces acting on the propeller, the wall must be immersed in the viscous sub-layer, with a $y^+ \approx 1$. To ensure this, the BL is meshed with a total thickness of 5 mm, 10 prism layers and 1.5 prism layer stretching.

4.2.3 Mesh independence study

To ensure the numerical solution is independent of the spatial discretization of the computational domain, a mesh independence study is conducted. This involves systematically refining the computational mesh and monitoring key parameters to determine the mesh resolution required to obtain a solution within an acceptable error band. Therefore, the goal is to reach an element size such that the results obtained are accurate enough without compromising the computational cost of the simulation. The element size is controlled through the Base Size of each mesh, leading to different meshes with varying numbers of elements. The parameter studied is the propulsive efficiency, η, analyzed for different values of the advance ratio, as shown in Table 4.3. The table also shows the efficiency values at the J with the greatest variation, along with the relative error between this and the value from the previous mesh. The results are shown in Figure 4.5 for a fixed rotational speed of 575 rpm.

Mesh #	**No. of cells [-]**	**Comp. time [h]**	**η [-]**	***error* [%]**
Mesh 0	400,000	0.58	0.0592	-
Mesh 1	800,000	2.37	0.0595	0.6148
Mesh 2	1,600,000	5.43	0.0575	3.5255
Mesh 3	3,200,000	12.09	0.0747	22.9801

Table 4.3: Summary of the mesh independence study results.

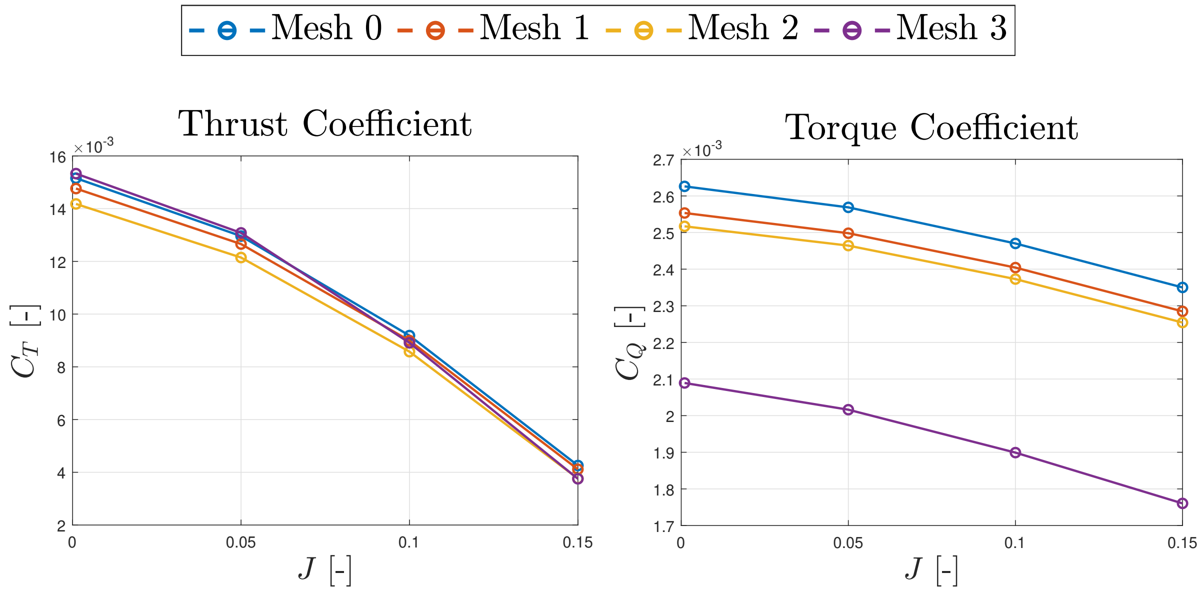

(a) Thrust coefficient.

(b) Torque coefficient.

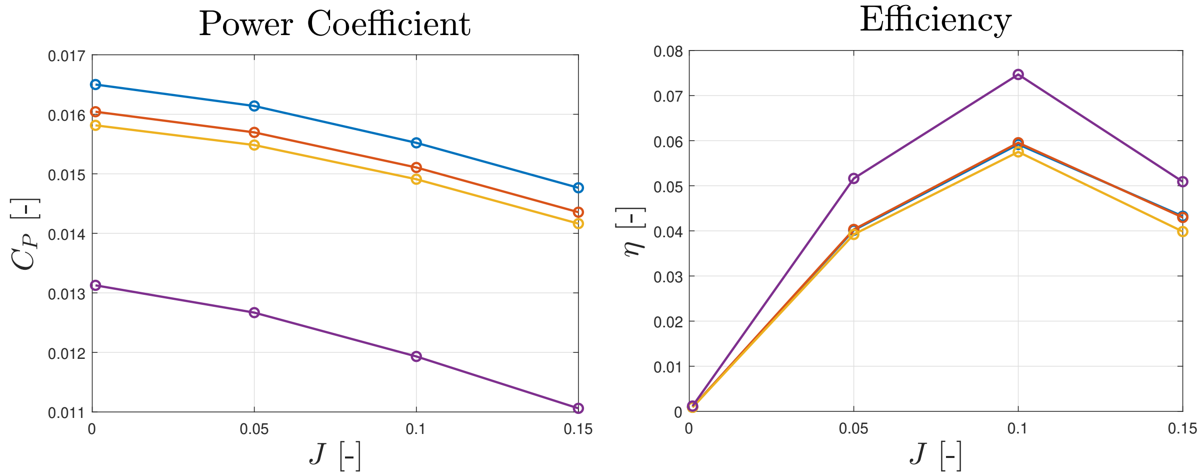

(c) Power coefficient.

(d) Propulsive efficiency.

Figure 4.5: Mesh independence study results. Performed at $\theta = 5°$ and $\Omega = 575$ rpm.

Based on the results of the aforementioned study, despite the values of C_Q (and consequently, C_P and η) presenting a higher variation in *Mesh 3*, this variation is not noticeable for C_T, which is the main parameter analysed in this project. Moreover, the increase in the total number of cells involved, significantly raises the computational cost of the simulations. Therefore, *Mesh 2* was selected due to its relationship between low relative error and lower computational cost compared to the subsequent refinements, since the volume of simulations requires an elevated total simulating time. Additionally, the y^+ values obtained for said mesh are predominantly lower than 1, as shown in Figure 4.6, indicating that the boundary layer lies within the viscous sublayer. Finally, Figure 4.7 represents the final mesh employed.

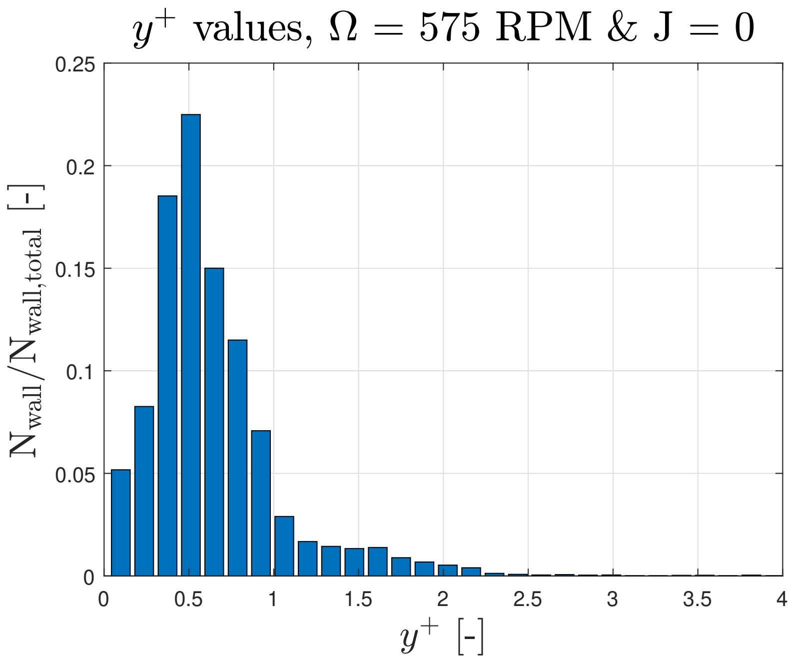

Figure 4.6: Histogram of y^+ values in the boundary layer cells for the final mesh.

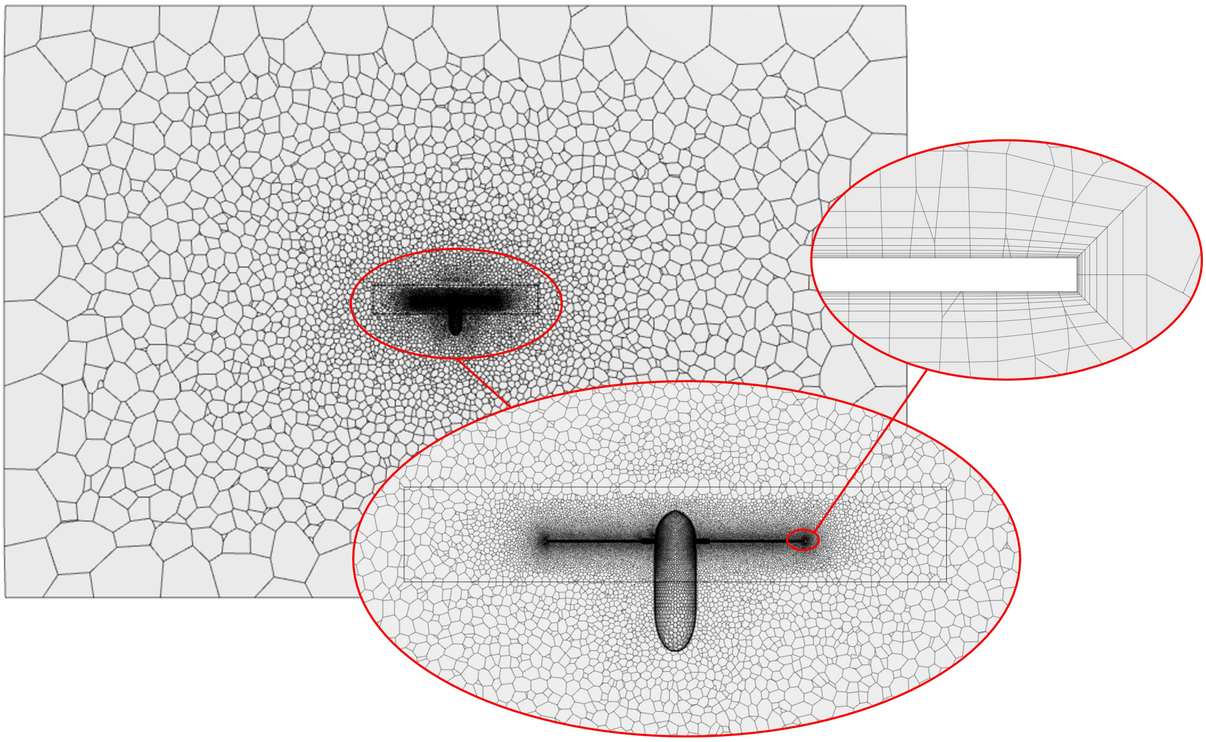

Figure 4.7: Final mesh cross-section. Details of the body and boundary layer.

4.2.4 Simulation Setup

The simulation set-up in *STAR-CCM+* must be appropriate for the case of study. With this statement, the following physical models, solver, and boundary conditions are selected:

- **Three-dimensional flow**. Due to the dimensions of the geometry, it is necessary to model the fluid in 3D.
- **Incompressible flow**. The flow is assumed to be incompressible as the flow velocity is significantly smaller than the speed of sound in the study conditions ($M < 0.3$).
- **Turbulent flow**. To evaluate the actual aerodynamic forces experienced by the propeller blades, it cannot be assumed that the fluid is inviscid. Therefore, the turbulence model $SST\ k-\omega$ is selected, as it provides reliable results near and far from the wall.
- **Steady flow**. The steady flow condition is used since the temporal variation of the solution is not studied.
- **Segregated flow**. As the flow is incompressible, segregated solver with 2nd order convection scheme is utilised because it yields faster convergence.
- **Flow properties**. Atmospheric conditions at sea level under normal conditions are established as follows:

Property	Value	Units
p_{ref}	101325	Pa
T_{ref}	300	K
ρ_{ref}	1.177	$\mathrm{kg/m^3}$
μ_∞	$1.855 \cdot 10^{-5}$	$\mathrm{Pa \cdot s}$
a_∞	347.28	m/s

Table 4.4: Flow properties at study conditions.

- **Boundary conditions.**
  - **Velocity inlet.** Because the flow is incompressible, the inlet condition is defined by the subsonic free-stream velocity.
  - **Pressure outlet.** For the outlet condition, it is specified that the pressure at the outlet equals the reference pressure.
  - **Slip-Wall.** The farfield of the computational domain is defined as a wall that has zero wall shear stress, meaning that the fluid can slide freely along the wall surface without any frictional resistance.
  - **Wall.** The body surface is assigned the wall boundary condition to model and mesh the effects of the boundary layer and the no-slip condition.
  - **Interface.** Finally, the interfaces between the rotatory zone and the fluid domain are defined.

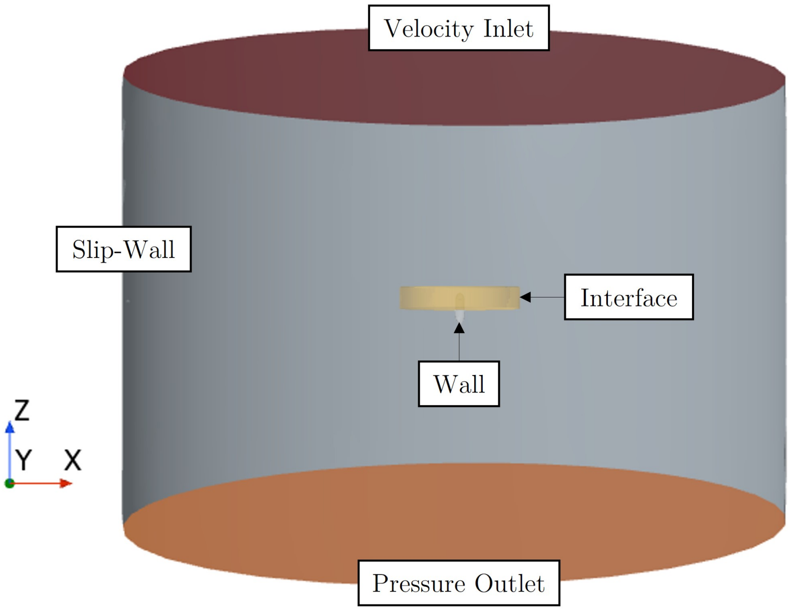

Figure 4.8: Boundary Conditions of the Computational Domain.

4.2.5 Motion simulation

To simulate the rotatory motion of the propeller, two distinct approaches could be followed:

- **Moving Reference Frame (MRF)**. The MRF (also known as *frozen rotor* approach) is a steady-state method in which the computational domain is divided into rotating and non-rotating regions. In the rotating region a constant angular velocity is imposed, although the mesh remains stationary. The governing equations are solved separately, while boundary conditions at the interfaces couple the solutions. MRF is computationally less expensive as it does not require time-dependent solutions, but also less accurate capturing transient phenomena and unsteady wake interactions.

- **Rigid Body Motion (RBM)**. The RBM is an unsteady method where the rotating region moves physically relative to the reference frame, according to the rotation of the propeller. The transient approach allows to capture unsteady phenomena and transient interactions, providing a more accurate representation of the real-world behavior of the propeller. It is also significantly more computationally intensive than the MRF approach due to the need for time-dependent solutions.

As stated before in this chapter, as the volume of simulations that need to be performed is substantial, the MRF approach is selected to simulate the rotation of the propeller.

4.2.6 Convergence criteria and validation

A critical step in obtaining accurate and reliable results from CFD simulations is ensuring numerical convergence. The iterative solution process must be allowed to continue until the numerical results have sufficiently converged, indicating that a steady-state or periodic solution has been reached. The primary indicators of convergence monitored during the simulations were the evolution of the residuals and the variables of interest.

The residuals provide a measure of the imbalance in the discretized governing equations at each iteration, and their reduction demonstrates the approach to a mathematically converged solution. Figure 4.9 shows the convergence history of the relative residuals for the continuity, momentum, and turbulence model equations. In this specific case, all residuals are observed to decrease by several orders of magnitude from their initial values, indicating a high degree of numerical convergence, and reaching stable low levels after approximately 1200 iterations.

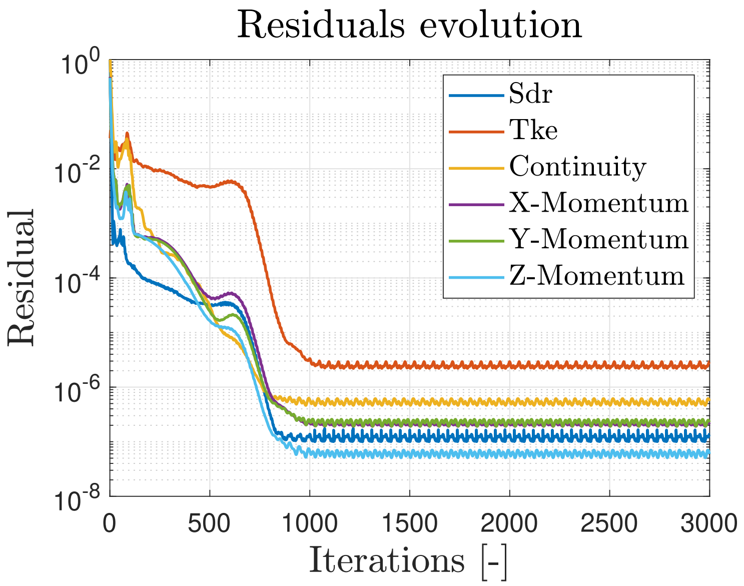

Figure 4.9: Example of residuals evolution during a certain simulation.

In addition to the residuals, the key output parameters of interest, such as the thrust and torque of the propeller, were also monitored for convergence. Figure 4.10 plots the evolution of Thrust as the simulation progressed. It is evident that these variables stabilized and reached constant values after around 1200 iterations, coinciding with the residuals reaching their low asymptotic levels.

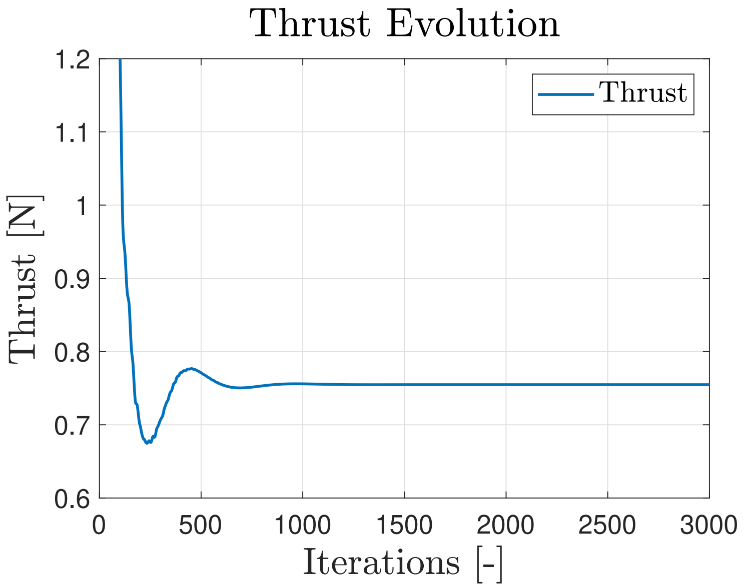

Figure 4.10: Example of thrust evolution during a certain simulation.

Chapter 5

Results

5.1 Introduction

This chapter presents the findings from the CFD analyses conducted to characterize the aerodynamic performance of the flat plate propeller. Firstly, the propeller's characteristic curves are determined, establishing the relationships between key performance parameters such as thrust, torque and rotational speed. These results are obtained through CFD simulations at a fixed blade pitch angle of 5 degrees. Building upon this, the influence of the propeller rotational speed and the blade thickness is studied. A series of CFD simulations are conducted to quantify how changes in these parameters impact the thrust generation of the propeller. Finally, a parametric study was performed to study the relationship between the blade pitch angle and the propeller's thrust coefficient, aiming to identify the optimal pitch setting for maximizing the thrust output.

The results from the different CFD studies are presented through a combination of graphical plots and flow visualization scenes. The trends observed are analyzed in the context of the underlying propeller aerodynamics principles to provide physical insights into the performance behavior.

5.2 Characteristic curves of the propeller

The primary objective of this study is to characterize the aerodynamic performance of the propeller by obtaining its characteristic curves and to verify the hypothesis that the thrust and torque coefficients are independent of the rotational speed, and consequently, the Reynolds number (determined from Equation 3.36). The characteristic curves of the propeller were obtained from the CFD simulations across a range of rotational speeds that can be found in Table 5.1.

The results obtained are shown in Figure 5.1. The maximum thrust and power coefficients are obtained at zero advance ratio as the induced velocity is maximum. As the advance ratio increases, the induced velocity drops and the coefficients values decrease. The maximum propulsive efficiency is given at $J = 0.1$. At this point, despite the thrust not being maximum, the power consumed by the propeller is reduced due to a decrease in the torque, leading to an equilibrium point of maximum efficiency.

Ω [rpm]	***n*** [rev/s]	***Re*** [-]
425	7.08	$4.05 \cdot 10^5$
575	9.58	$5.49 \cdot 10^5$
750	12.5	$7.16 \cdot 10^5$

Table 5.1: Range of rotational speed and Reynolds number analysed in the characteristic curves study.

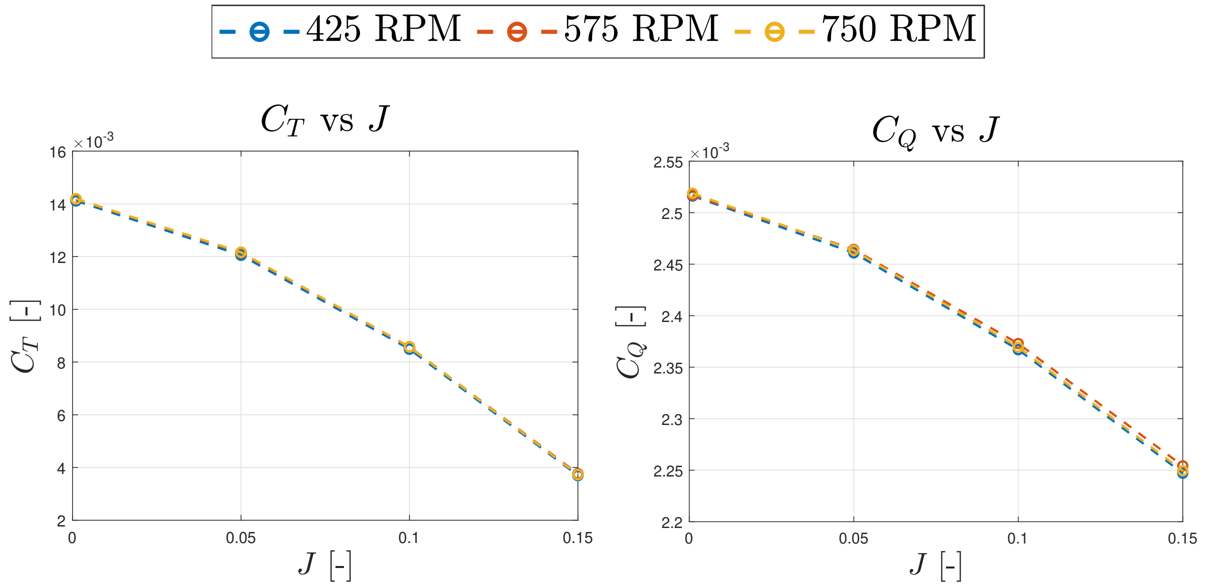

(a) Thrust coefficient

(b) Torque coefficient

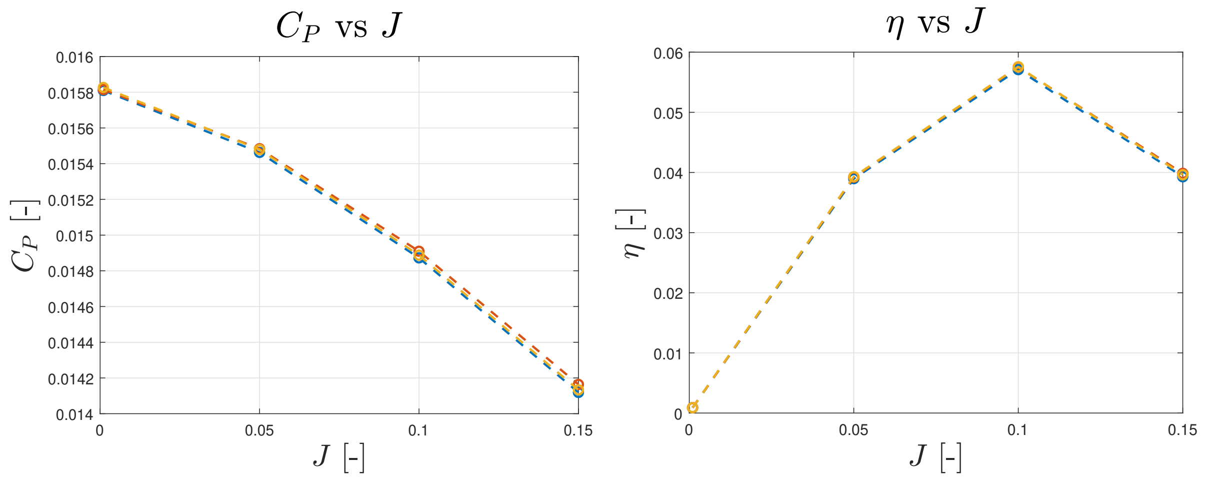

(c) Power coefficient

(d) Propulsive efficiency

Figure 5.1: Characteristic curves of the propeller as a function of the advance ratio for different rotational speeds. Performed at $\theta = 5°$.

The graphs clearly indicate that the aerodynamic performance of the propeller is indeed independent of the rotational speed, and consequently, of the Reynolds number. The observed independence can be attributed to the geometric similarity and flow similarity conditions maintained across different rotational speeds. Since the propeller operates in a turbulent regime where the flow characteristics are governed primarily by inertial forces rather than viscous forces, the Reynolds number has a negligible effect on the non-dimensional performance coefficients. This finding is significant as it simplifies the analysis and design of propellers by allowing the use of non-dimensional coefficients regardless of the operating conditions.

Figure 5.2 shows the non-dimensional velocity contours around the blade section at $r = 0.8$ (recall that $r = y/R$) for the different rotational speeds analysed in this study. The non-dimensional velocity is calculated following Equation 5.1 and is expressed in the rotating reference frame. It can be easily observed that, since the non-dimensional velocity is non-dimensionalized with Ω, the contours of different rotational speeds seem to not vary significantly. In a similar way, the non-dimensional coefficients are demonstrated to be independent of Ω and Re.

$$V^*_{rot} = \frac{V_{rot}}{\sqrt{\left(\Omega\sqrt{x^2+y^2}\right)^2 + (JnD)^2}} \tag{5.1}$$

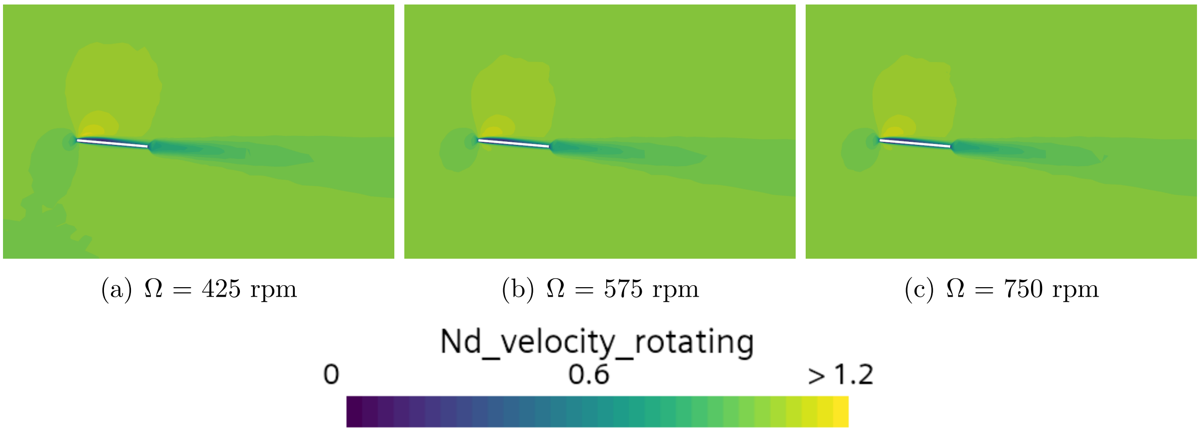
(a) $\Omega = 425$ rpm (b) $\Omega = 575$ rpm (c) $\Omega = 750$ rpm

Figure 5.2: Non-dimensional velocity contours for different rotational speeds, at $r = 0.8$, $\theta = 5°$ and $J = 0.1$.

In Figure 5.3, the pressure coefficient distribution along the blade chord is shown for the different values of advance ratio analysed. The results correspond to the section of the blade located at $r = 0.65$ and a value of rotational speed of $\Omega = 575$ rpm. The pressure coefficient analysed is calculated following Equation 5.2. It represents the non-dimensional pressure distribution, where the dynamic pressure is calculated with the relative velocity *seen* by each section of the blade. The figure shows how the pressure distribution along the chord presents a similar behaviour for every advance ratio studied. It is observed that the distribution gets narrower as the advance ratio increases, making the pressure difference between the pressure and suction sides lower.

$$Cp_{rot} = \frac{p - p_\infty}{\frac{1}{2}\rho_\infty[(\Omega y)^2 + (JDn)^2]} \tag{5.2}$$

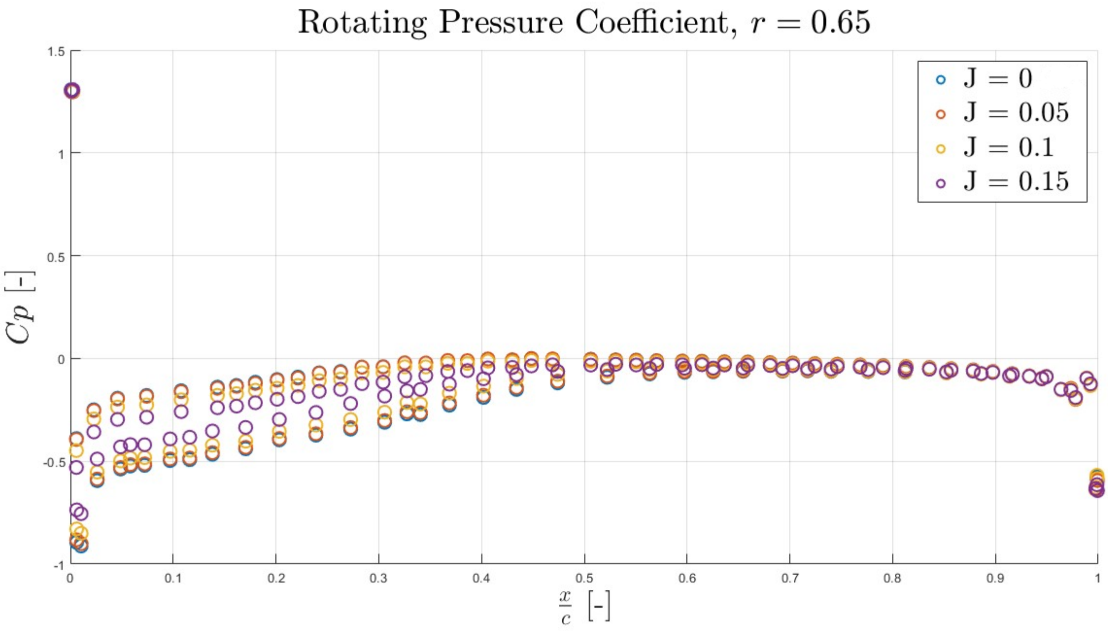

Figure 5.3: Comparison of the pressure coefficient distribution for different values of advance ratio, at $r = 0.65$, $\Omega = 575$ rpm and $\theta = 5°$.

Finally, Figure 5.4 shows the velocity downwash at the point of maximum efficiency and a rotational speed of 575 rpm.

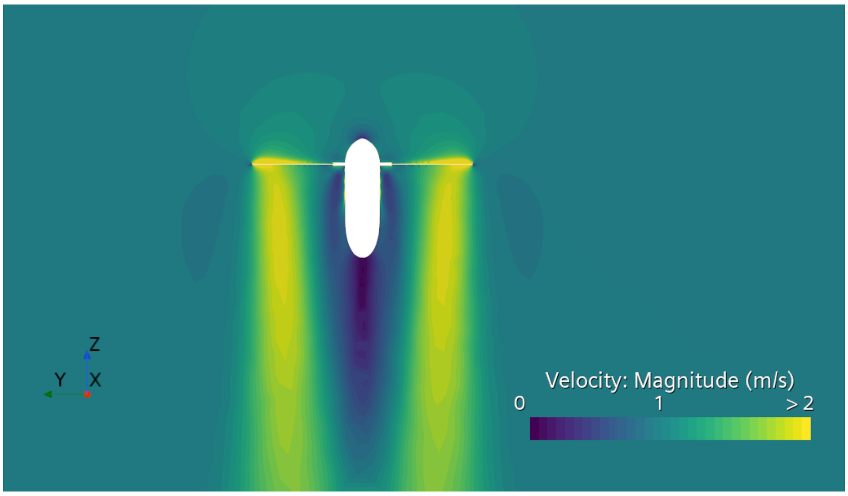

Figure 5.4: Velocity downwash at $J = 0.1$, $\Omega = 575$ rpm and $\theta = 5°$.

5.3 Study of the influence of the rotational speed.

To study the influence of the rotational speed on the generated thrust and torque is key in the determination of the propeller performance. Based on chapter 3, it is expected that the thrust and torque should scale approximately with the square of the rotational speed ($T \propto \Omega^2$ and $Q \propto \Omega^2$), following Equation 5.3. To validate this relationship, a series of CFD simulations are conducted at different propeller rotational speeds, Ω. The range of rotational speeds of this study can be seen at Table 5.2.

Ω [rpm]	n [rev/s]	Re [-]
300	5.00	$2.86 \cdot 10^5$
425	7.08	$4.05 \cdot 10^5$
575	9.58	$5.49 \cdot 10^5$
700	11.67	$6.68 \cdot 10^5$
900	15.00	$8.59 \cdot 10^5$

Table 5.2: Range of rotational speed and Reynolds number for the influence of the rotational speed study.

$$T = \frac{\rho D^4}{3600} C_T(J)\Omega^2, \qquad Q = \frac{\rho D^5}{3600} C_Q(J)\Omega^2 \tag{5.3}$$

Figure 5.5 shows the variation of thrust and torque with the propeller rotational speed at hovering conditions. The results clearly demonstrate the quadratic relationship between these quantities. Besides, a best-fit curve fitted to the CFD data points shows an exponent of 2 on the rotational speed, and a R^2 value equal to 1; agreeing completely with the expected theoretical values.

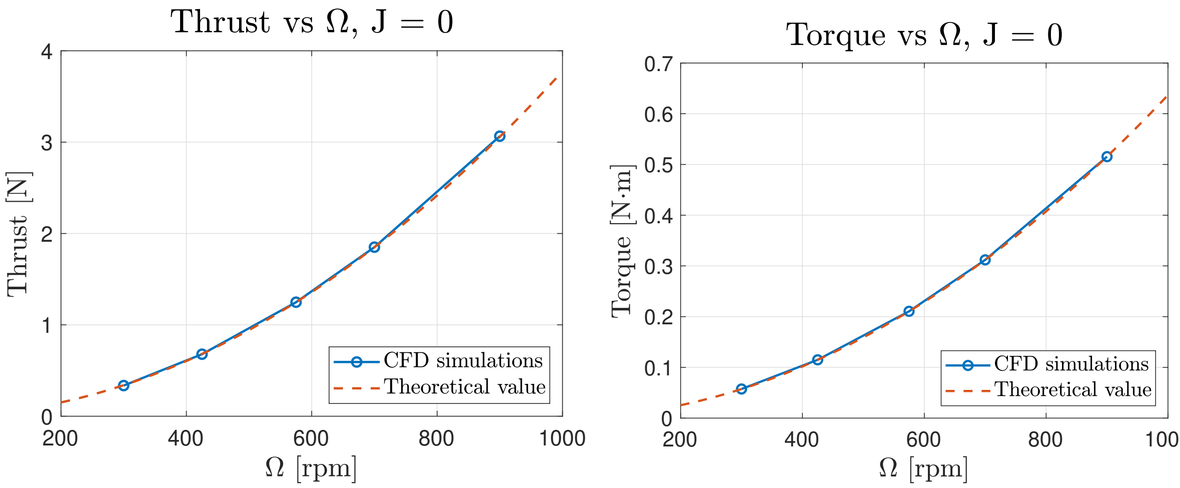

(a) Thrust

(b) Torque

Figure 5.5: Effect of the rotational speed on the thrust generated and torque, performed at $\theta = 5°$ and $J = 0$.

5.3.1 Influence of the blade thickness

It is also interesting to study the effect of blade thickness on the thrust force and torque generated. To do so, the previous analysis is repeated for a propeller with a blade of double the thickness, resulting in $h = 3.14$ mm. The consequent analysis verifies that both variables again follow a quadratic relationship with rotational speed. The values obtained for both thicknesses are shown in Figure 5.6.

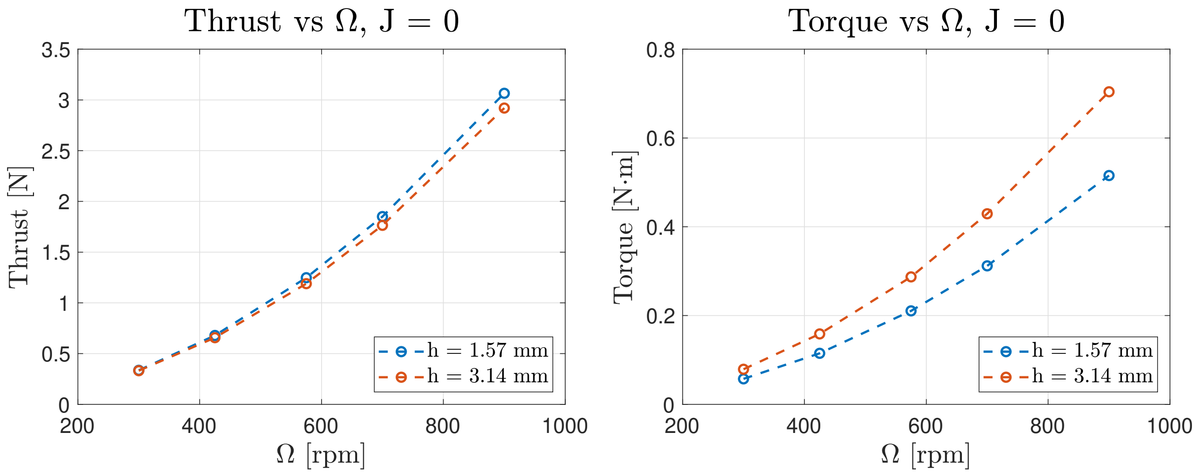

(a) Thrust (b) Torque

Figure 5.6: Comparison of thrust generated and torque for different blade thicknesses as a function of rotational speed, performed at $\theta = 5°$ and $J = 0$.

From the comparison represented in the graphs above, it can be extracted that the thrust force generated is almost independent on the blade thickness for low values of Ω. At higher values, from 575 rpm, the absolute difference seems to be increased as the rotation gets faster, being the thinner blade the one able to generate higher thrust. Nonetheless, the torque is more reactive to the blade thickness. Despite following the same behaviour as the thrust, presenting a lower absolute difference at low rotational speeds, the relative difference between the values is kept almost constant at around 37%. By comparing the non-dimensional velocity contours in Figure 5.7, it is clearly observed that the flow presents no substantial difference regardless of the blade thickness.

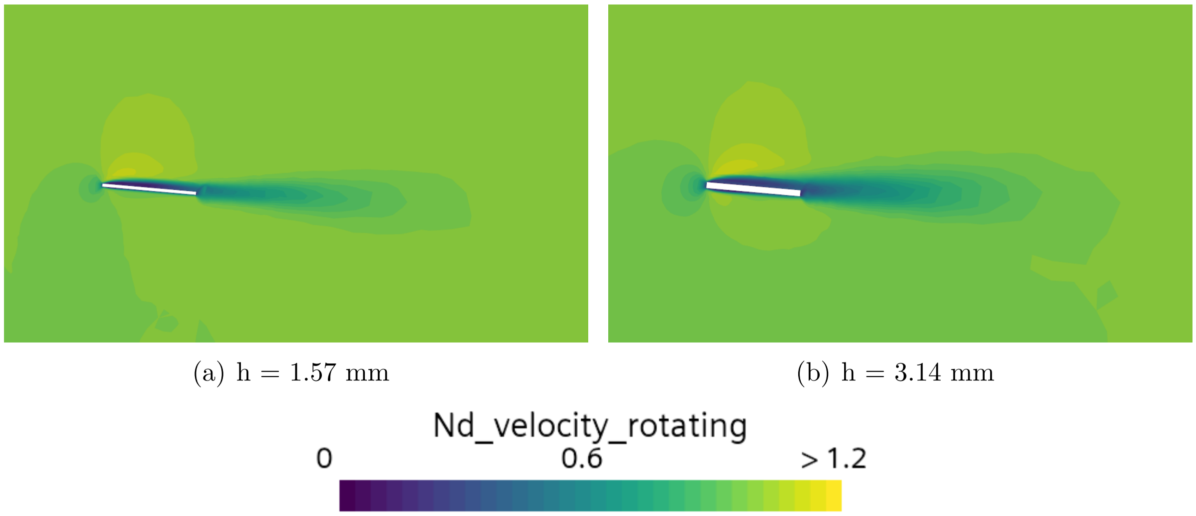

(a) h = 1.57 mm (b) h = 3.14 mm

Figure 5.7: Non-dimensional velocity contours at $r = 0.95$ for both thicknesses.

The pressure coefficient distribution along the blade chord, obtained for different sections of the blade is compared in Figure 5.8. From the plots it is observed how the pressure distribution on the thicker blade does not seem to vary much, except for a lower pressure zone close to the leading edge which disappears around the 30% of the chord.

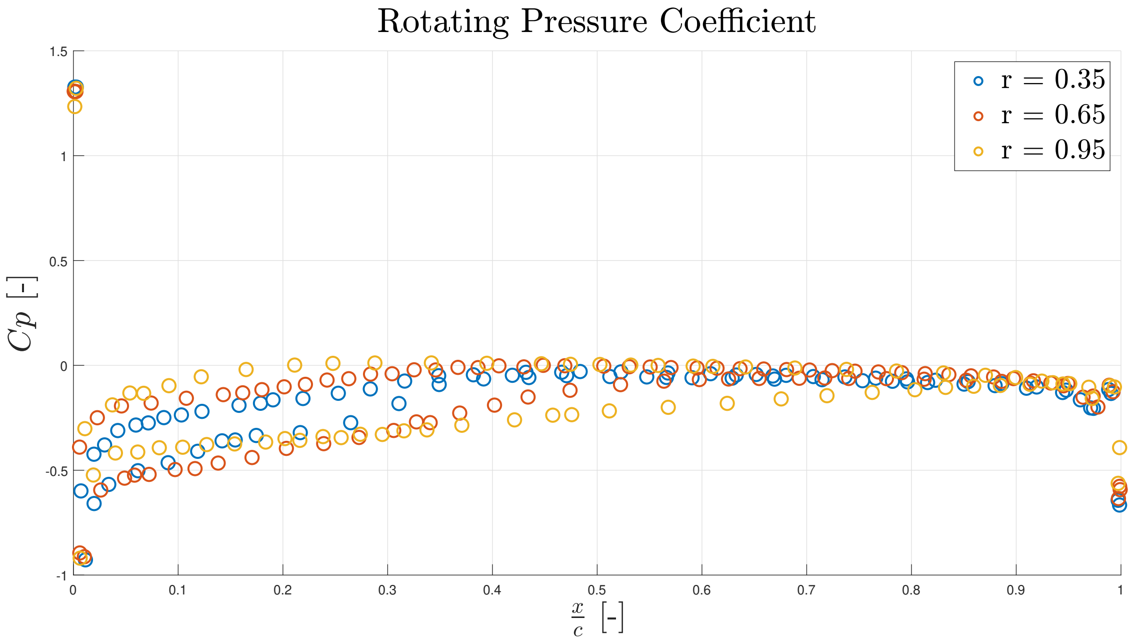

(a) h = 1.57 mm

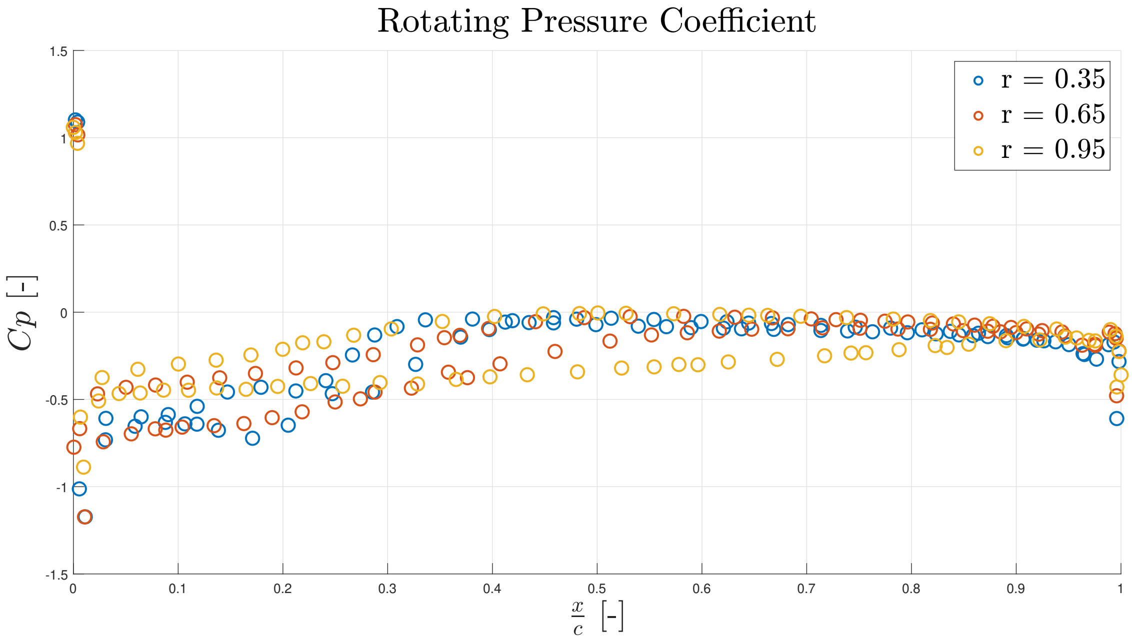

(b) h = 3.14 mm

Figure 5.8: Comparison of the pressure coefficient distribution for two different blade thicknesses, at various r distances. Performed at $\Omega = 575$ rpm and $\theta = 5°$.

The thrust is thus almost equal in both blades, as the lift force does not get affected. Figure 5.9 shows the pressure coefficient contours for both blade thicknesses at the section $r = 0.35$. Here, the same conclusion can be extracted. The thrust force generated is not affected by the blade thickness as the pressure distribution around the blade is very similar.

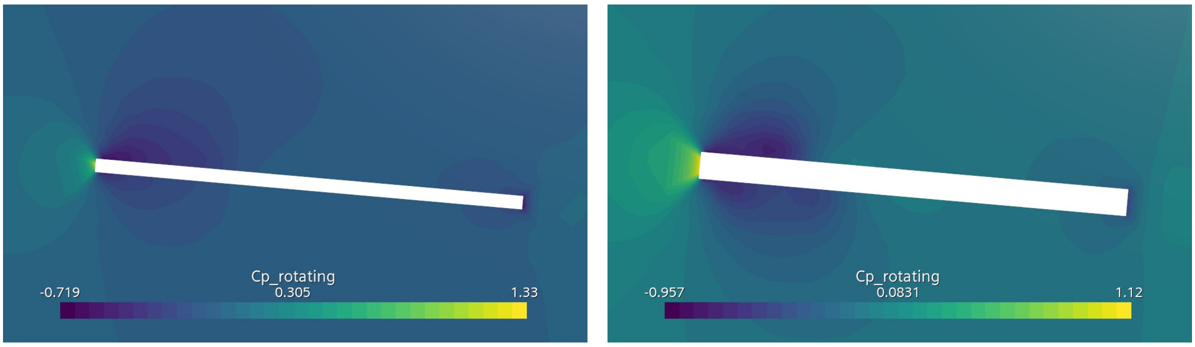

(a) h = 1.57 mm

(b) h = 3.14 mm

Figure 5.9: Pressure coefficient contours at $r = 0.35$ for both thicknesses.

5.4 Study of the influence of the pitch angle

The pitch angle of the propeller blades is a critical parameter that significantly influences the aerodynamic performance of the propeller. In this section, the relationship between the blade pitch angle, θ, and the thrust and torque coefficients is investigated. The study aims to determine the optimal pitch angle that maximizes thrust generation providing a better understanding on the aerodynamic behavior of the propeller at various pitch settings. The set of simulations are run at an advance ratio of $J = 0.1$, which corresponds to the point of maximum efficiency at $\theta = 5°$, obtained in section 5.2, and a rotational speed of $\Omega = 575$ rpm. The relationship between the blade pitch angle and the thrust coefficient was studied by varying the pitch angle from -5 degrees to 45 degrees in increments of 5 degrees. The thrust coefficients obtained from the CFD simulations for each pitch angle are visualized in Figure 5.10.

The results highlight a clear trend in the relationship between blade pitch angle and thrust coefficient. The C_T increases with the pitch angle, reaching a peak value at 40 degrees. Beyond this point, the thrust coefficient begins to decrease. This behavior can be explained by considering the aerodynamic principles governing the propeller's performance explained in the fundamentals chapter. As the pitch angle increases, the aerodynamic angle of attack of the blades also increases, resulting in a greater lift force generated by each blade. This lift force translates into higher thrust, thereby increasing the thrust coefficient. The increase in C_T with θ up to 40 degrees indicates that the flow remains attached to the blade surfaces and minimizes flow separation. At pitch angles greater than 40 degrees, the angle of attack becomes excessively high, leading to flow separation and stall on the blade surfaces. This causes a dramatic loss in lift and an increase in drag, resulting in a reduction of the thrust. Similarly, the propulsive efficiency presents its maximum at 10 degrees, and drops after this value of pitch angle. Before this point, the power consumed by the propeller does not grow as fast as the thrust generated does. However, from this point, in spite of the thrust still increasing, the torque at the rotor grows faster, creating the decrease in propulsive efficiency. The non-dimensional velocity contours around the blade for the angle of maximum efficiency are displayed at different span sections in Figure 5.11. It is observed that the flow increases the separation from the blade surface in the sections closer to the blade tip. Below, Figure 5.12 represents the pressure coefficient along the blade suction side.

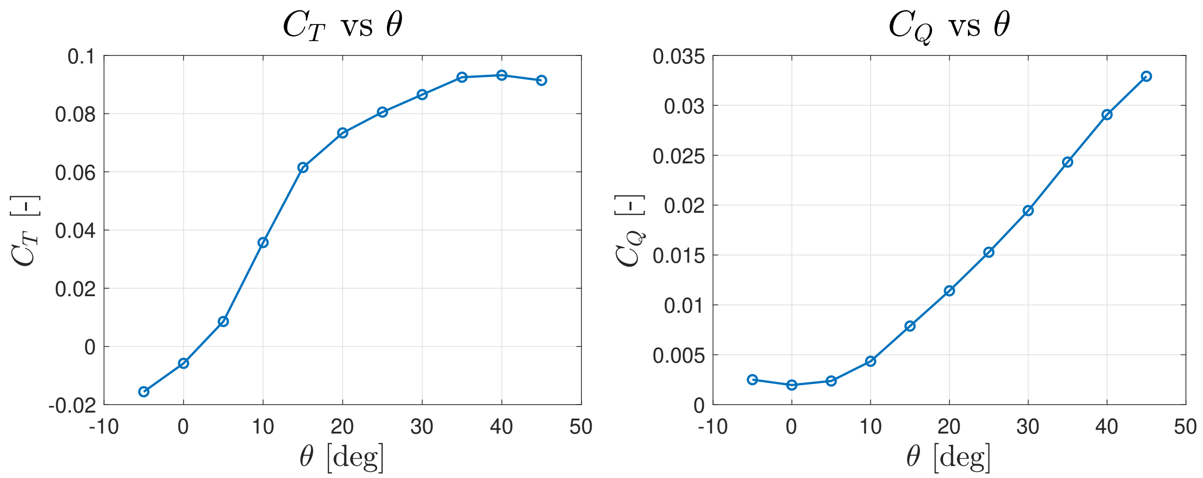

(a) Thrust coefficient (b) Torque coefficient

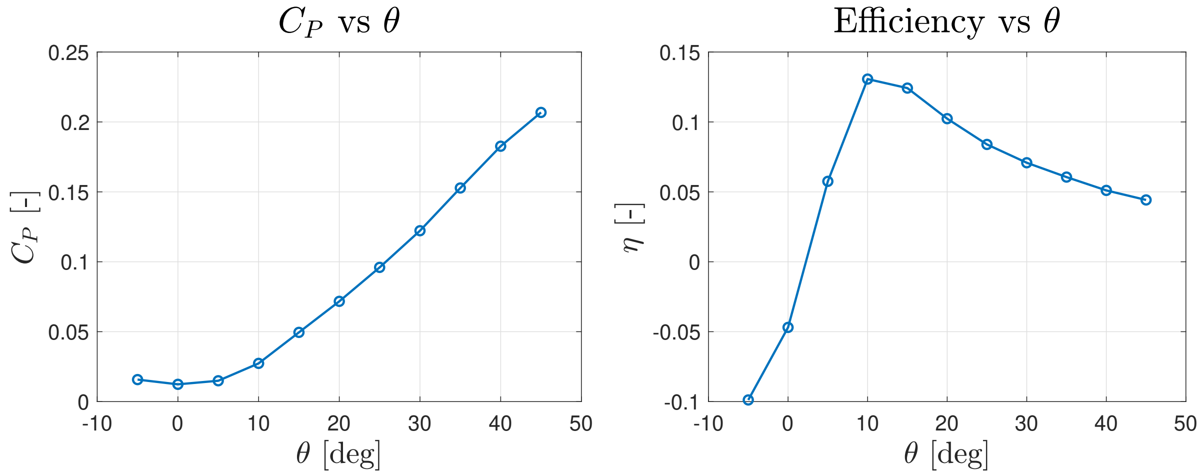

(c) Power coefficient (d) Propulsive efficiency

Figure 5.10: Pitch angle parametric study results, performed at $J = 0.1$.

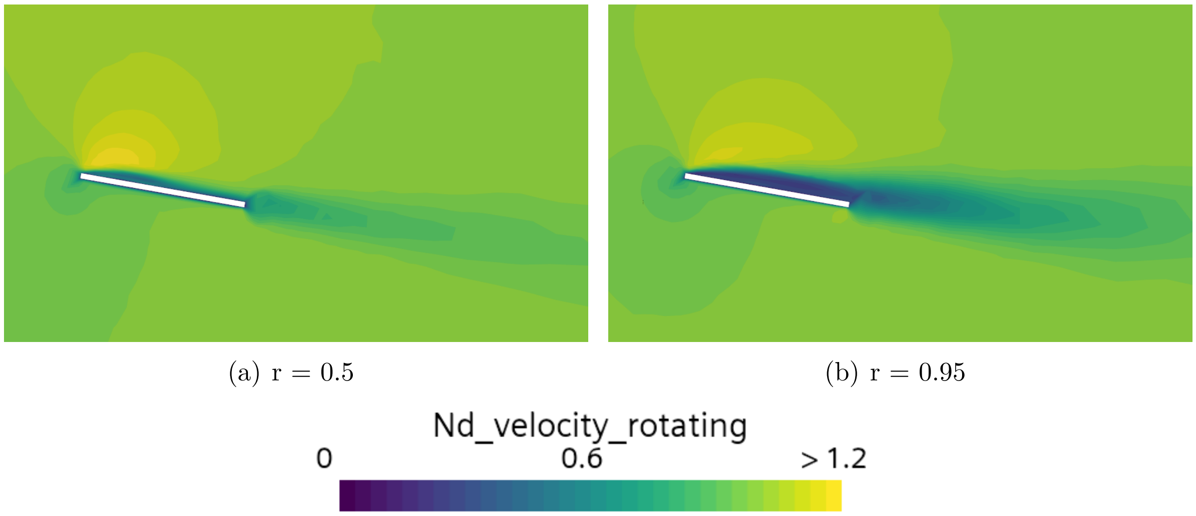

(a) r = 0.5 (b) r = 0.95

Figure 5.11: Non-dimensional velocity contours at $\theta = 10°$ and $J = 0.1$.

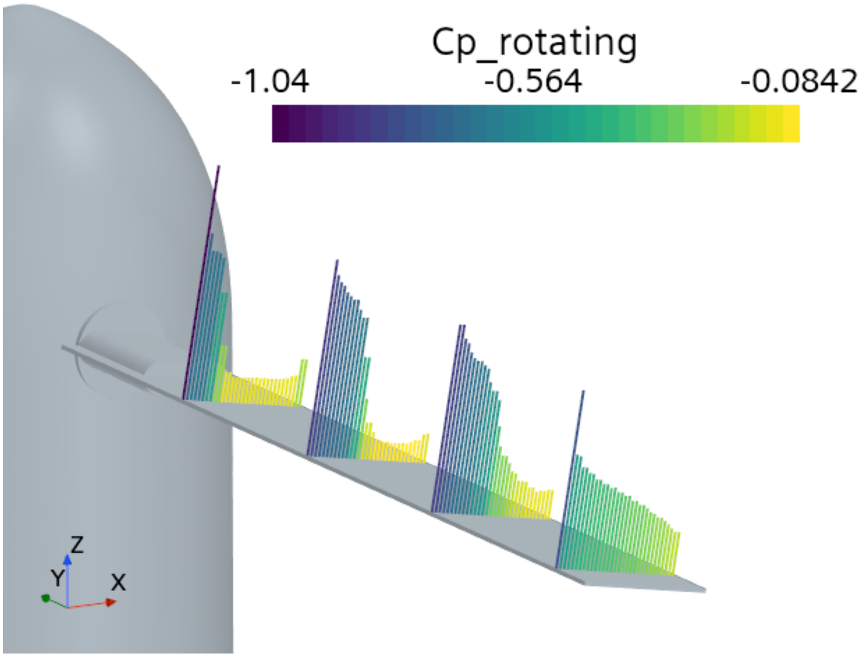

Figure 5.12: Pressure coefficient distribution over the blade suction side at $\theta = 10°$.

Next, Figure 5.13 shows the velocity contours around the blade at 40 degrees. By comparing this with the previous figures at 10 degrees, it is observed how a significantly bigger region of the flow field is accelerated, resulting in a greater pressure difference and thus, in a greater thrust force generated. Besides, the flow is now much more separated, especially at the tip sections, causing an increase in the drag force. The pressure difference can also be observed in Figure 5.14, where it is easily noticeable that the pressure coefficient distribution, especially at the sections closer to the blade root, takes values much lower at higher pitch angles.

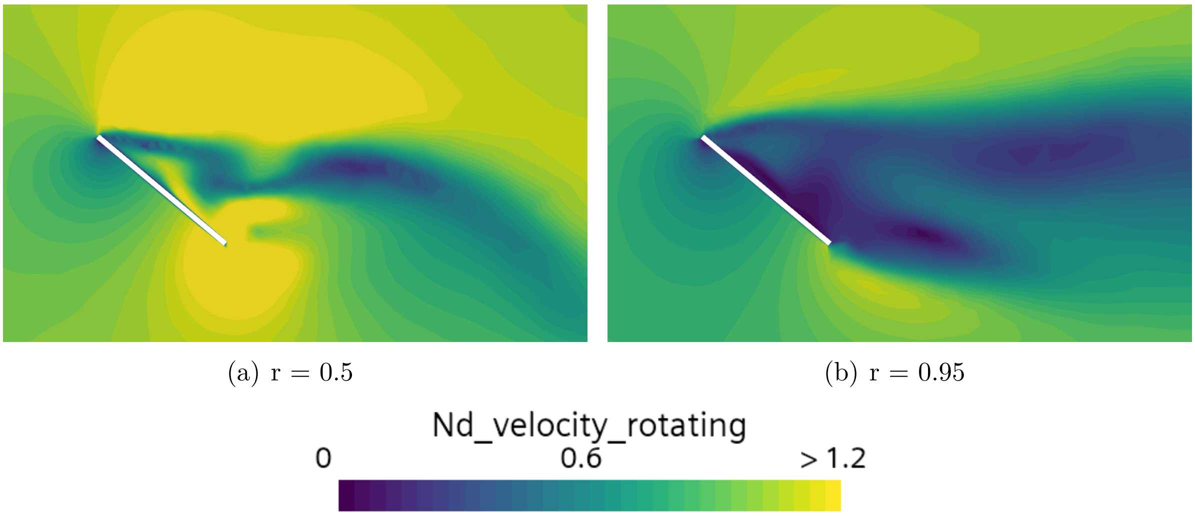
(a) r = 0.5

(b) r = 0.95

Figure 5.13: Non-dimensional velocity contours at $\theta = 40°$ and $J = 0.1$.

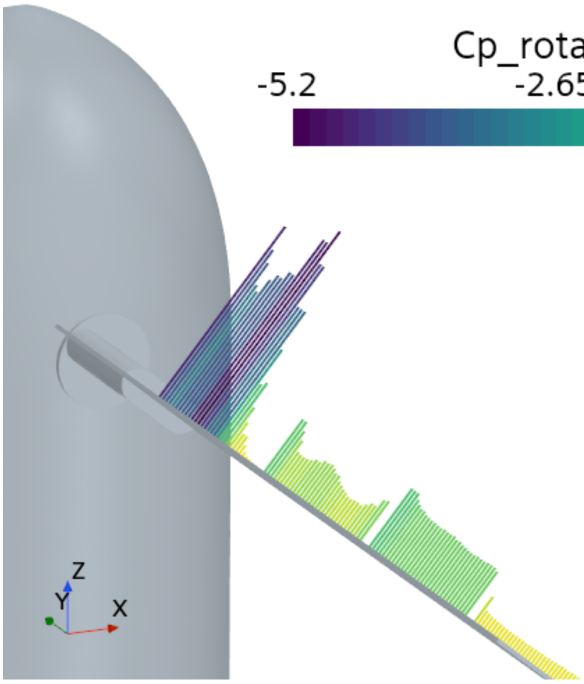

Figure 5.14: Pressure coefficient distribution over the blade suction side at $\theta = 40°$.

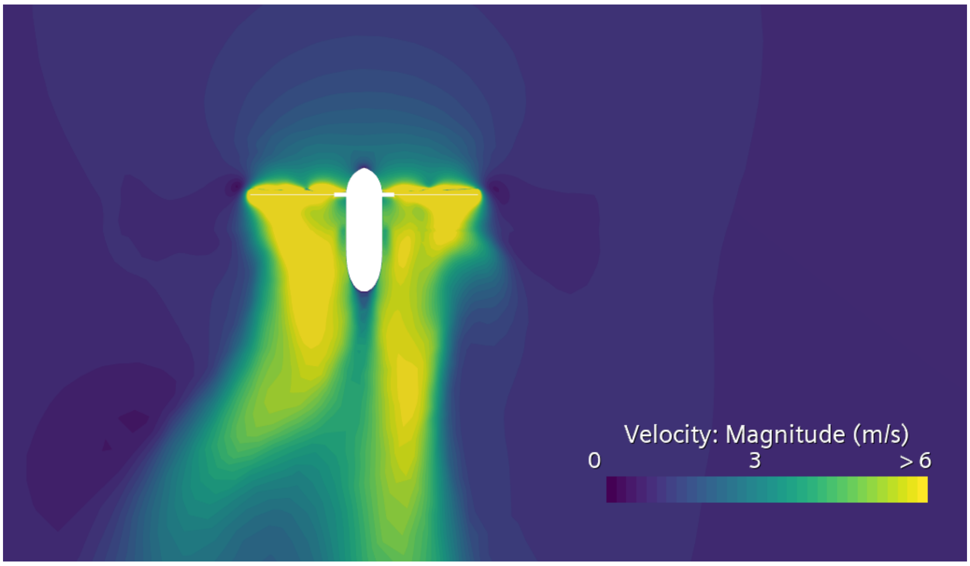

Figure 5.15: Velocity downwash at $\theta = 40°$ and $J = 0.1$.

The same study is now repeated but in hovering conditions of $J = 0$. The results appear in Figure 5.16. This time, the study is performed varying the pitch angle from 0 degrees to 40 degrees in increments of 10 degrees. Although with less resolution, the curves show very similar trends as in the previous analysis. The torque coefficient increases monotonically in the range analysed. Likewise, the thrust coefficients presents its maximum value this time at $\theta = 30$ degrees, from which it starts to decrease. Moreover, this value is 13% lower than the value obtained with an advance ratio of $J = 0.1$.

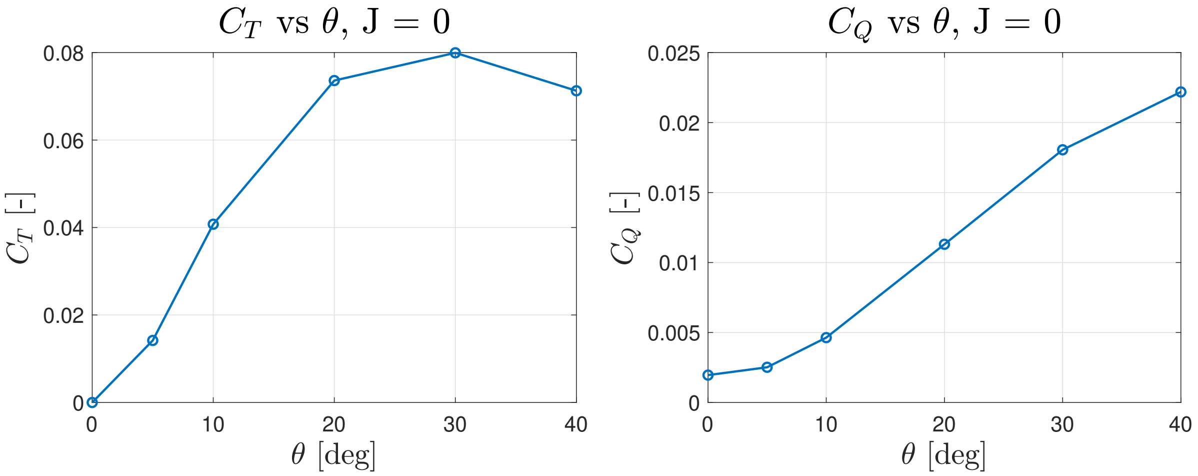

(a) Thrust coefficient (b) Torque coefficient

Figure 5.16: Pitch angle parametric study results, performed at $J = 0$.

As a comparison with the previous analysis, the velocity contours around the blade at a pitch angle of 40 degrees are represented in Figure 5.17. The figures show that in the case of hovering flight, for high pitch angles, the velocity field is less accelerated, leading to a decrease in the total thrust generated. Looking at the wake, this one results to be thinner. For a more detailed analysis, the pressure coefficient distribution plot for both values of advance ratio and $\theta = 40°$, are found in the following Figure 5.18. It is appreciated how the pressure drops lower in the middle sections at $J = 0.1$. Lastly, the pressure drops at the section $r = 0.35$ in both cases is similar though for $J = 0$, it is given closer to the leading edge.

Figure 5.19 shows the velocity downwash for a pitch angle of 40 degrees and $J = 0$. By comparing it with Figure 5.15, it might be observed that the induced velocity at $J = 0.1$ presents higher values further into the wake than in hovering conditions, explaining the thrust loss as well.

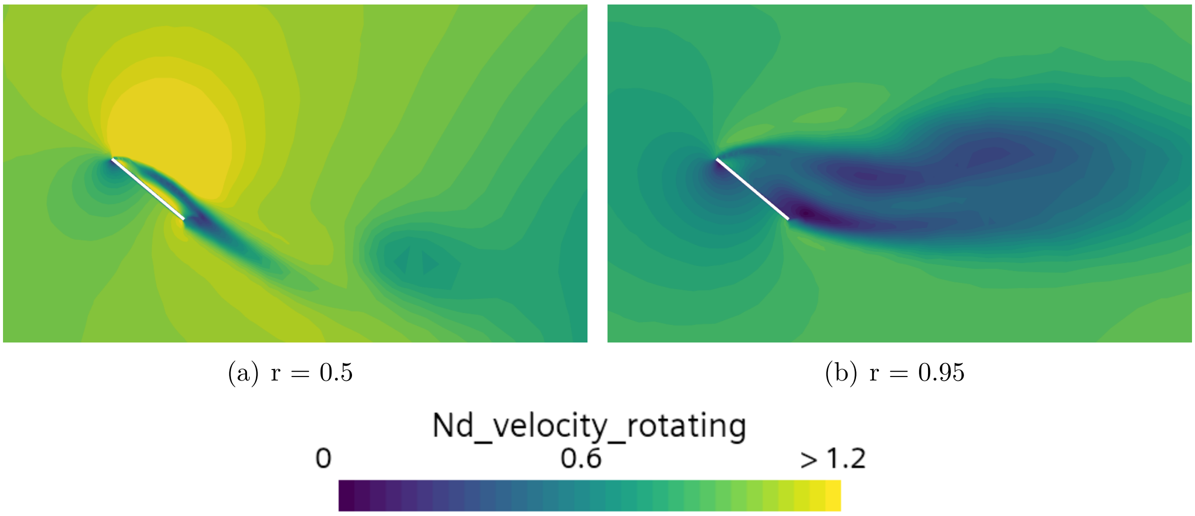

(a) r = 0.5 (b) r = 0.95

Figure 5.17: Non-dimensional velocity contours at $\theta = 40°$ and $J = 0$.

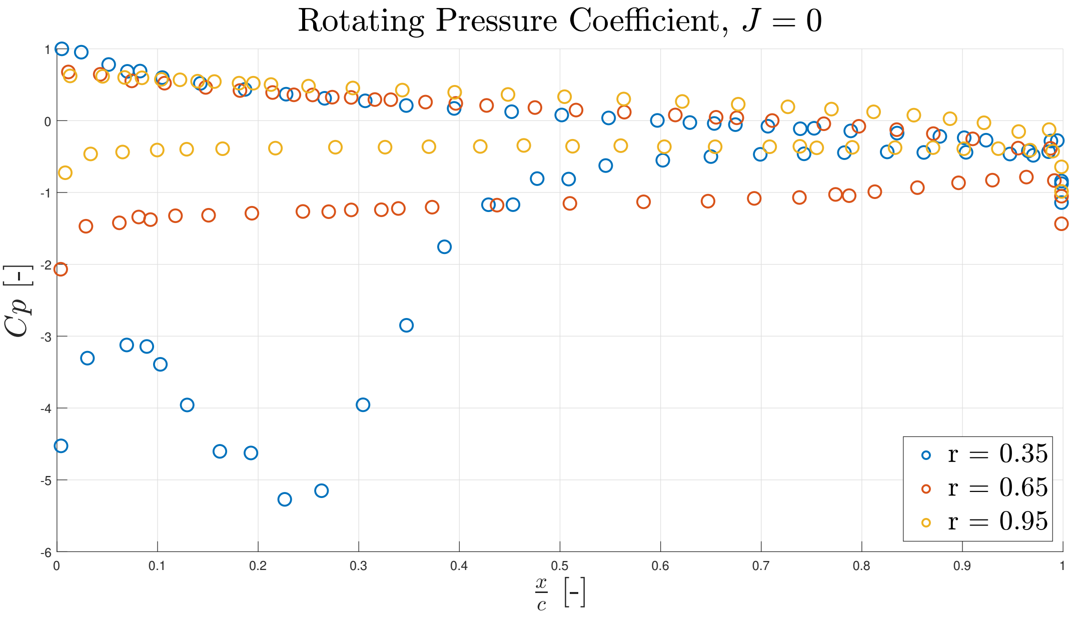

(a) $J = 0$

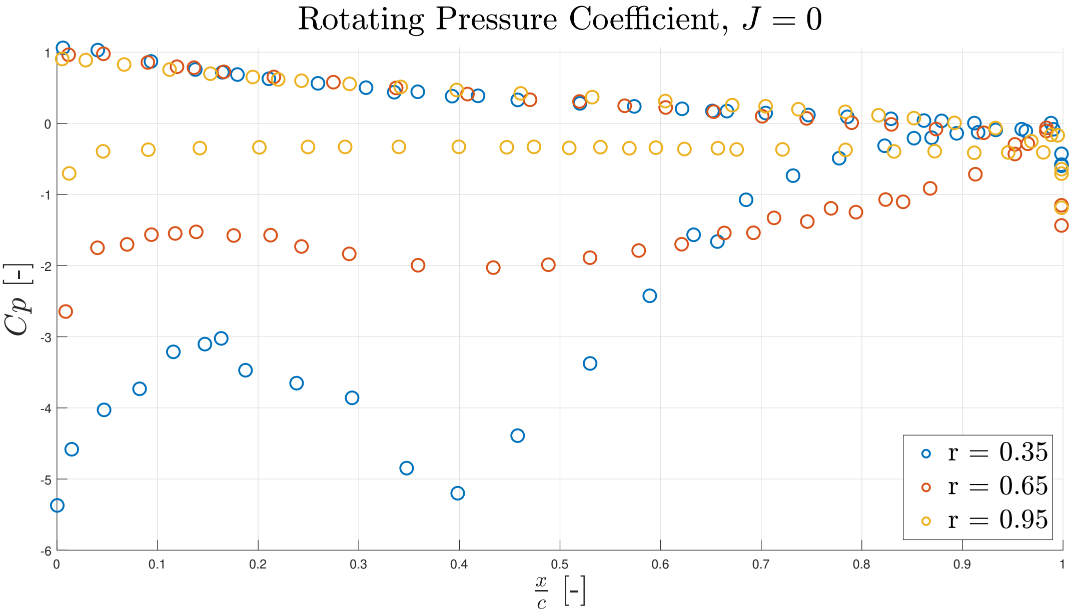

(b) $J = 0.1$

Figure 5.18: Comparison of the pressure coefficient distribution at various r distances for different values of advance ratio. Performed at $\Omega = 575$ rpm and $\theta = 40°$.

The results demonstrate that the thrust coefficient increases with the pitch angle up to an optimal point, beyond which further increase in pitch angle lead to a decrease in thrust due to flow separation and stall. These findings are crucial for the design and operation of propellers, as they suggest that an optimal pitch angle exists for maximizing thrust generation. Besides, operating the propeller at pitch angles beyond the point of maximum efficiency, can significantly reduce performance. For a final and clearer comparison, Figure 5.20 shows together the thrust and torque coefficients for the two values of J analysed.

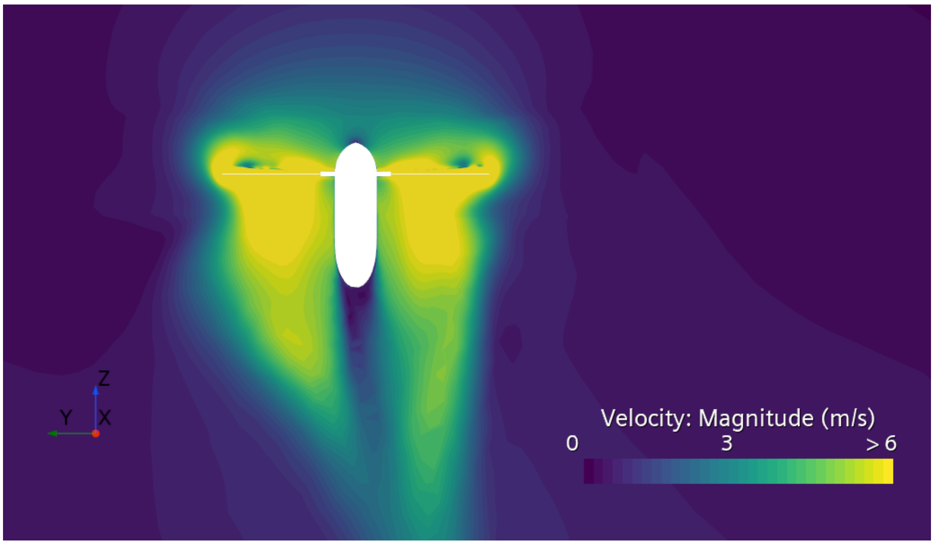

Figure 5.19: Velocity downwash at $\theta = 40°$ and $J = 0$.

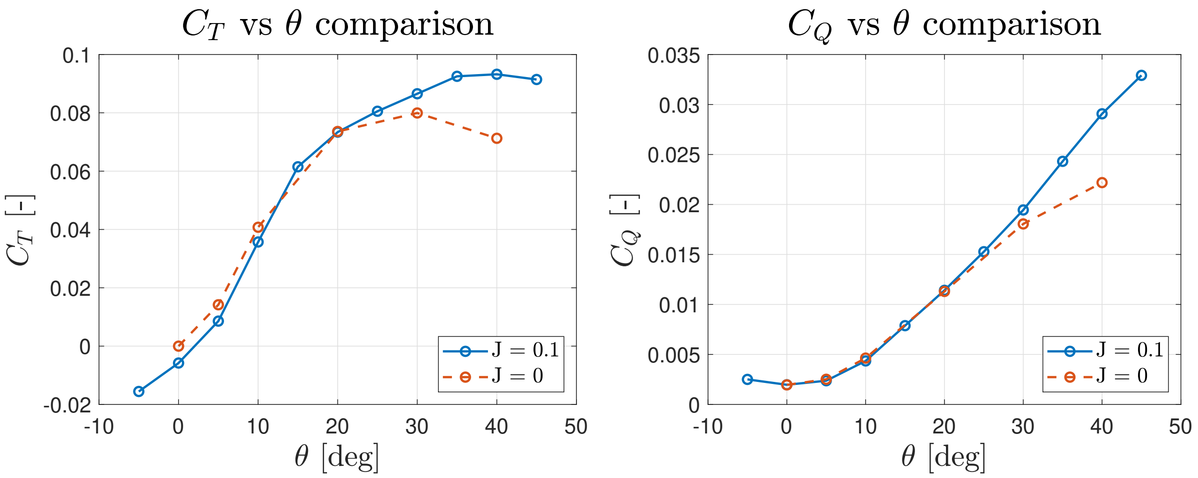

(a) Thrust coefficient

(b) Torque coefficient

Figure 5.20: Comparison of the thrust and torque coefficients for different values of J.

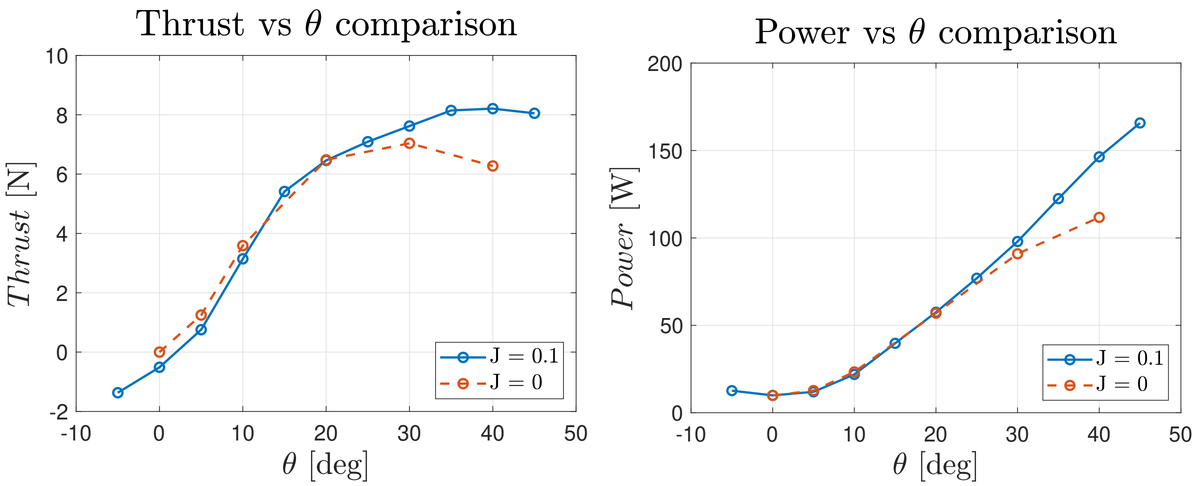

(a) Thrust

(b) Power

Figure 5.21: Comparison of the thrust and power for different values of J.

In Figure 5.21 above, the dimensional thrust force generated by the propeller and the power needed are compared as well. The observed behavior in the thrust and power graphs can be attributed to several aerodynamic factors. First, the thrust seems to increase with the pitch angle until a certain point where it starts to stabilize or even decrease. In the case of $J = 0$, this occurs earlier at around $\theta = 20°$, whereas in $J = 0.1$, the phenomenon is delayed until $\theta = 35°$. The reason of this is the fact that after that specific pitch angle, the wake generated is very similar in shape and direction, and so, the thrust force is not further increased. This is shown in the following Figure 5.22. Finally, the power consumed appears to keep increasing in both cases despite the thrust stabilizing. This fact is explained by considering that the rise in thrust as a consequence of an increase in the lift force, implies a rise in the drag force as well. Thus, the propeller's power needs to be augmented to overcome the resistance. When the thrust stops increasing, the power keeps growing as the wake becomes completely turbulent, maximizing the drag and energy losses. Also, before the point at $\theta = 20$ degrees, both values of advance ratio result in the same values of power, as it was observed from the torque coefficient analysis. From this point, the power reduces its growing ratio in the hovering case.

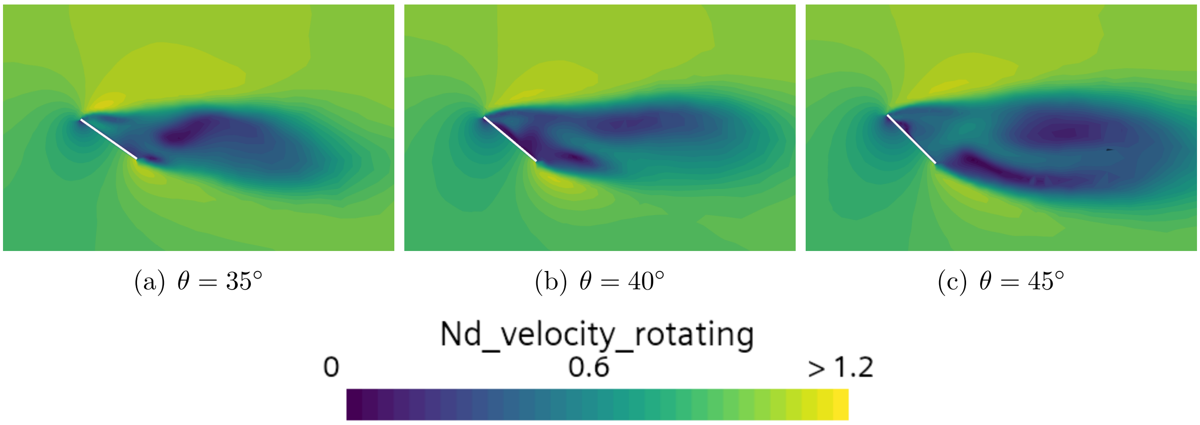
(a) $\theta = 35°$ (b) $\theta = 40°$ (c) $\theta = 45°$

Figure 5.22: Non-dimensional velocity contours for different pitch angles, at $r = 0.95$ and $J = 0.1$.

Chapter 6

Conclusions and future work

6.1 Conclusions

This chapter, provides a comprehensive summary of the key findings and achievements in relation to the stated objectives and their implications. Overall, the CFD-based investigations presented herein have led to an understanding of the propeller performance characteristics.

The study began with a thorough review of the fundamental principles underlying CFD simulations and rotor aerodynamics. Key concepts such as the thrust coefficient (C_T), torque coefficient (C_Q), and the main theories that explain the aerodynamic behaviour of propellers were defined and discussed. This foundational understanding was crucial for setting up accurate simulations and interpreting the results. By employing the Moving Reference Frame (MRF) quasi-stationary approach, the simulations captured the essential aerodynamic characteristics of the propeller with acceptable accuracy, while maintaining low computational resource usage.

The research into the influence of the rotational speed on the propeller's non-dimensional parameters revealed that both the thrust coefficient and torque coefficient, and thus the propulsive efficiency, are independent of the Reynolds number. This finding was consistent across a range of rotational speeds, confirming the hypothesis that the aerodynamic performance of the propeller is primarily governed by inertial forces rather than viscous effects. This independence simplifies the analysis and design of propellers, as the non-dimensional coefficients can be used universally across different operating conditions.

The study of the effect of rotational speed on thrust and torque generation confirmed the expected quadratic behaviour given by the theory. Additionally, the influence of blade thickness on performance was analyzed, indicating that while thicker blades might provide structural advantages, their aerodynamic performance needs careful optimization to avoid unnecessary drag increases.

Finally, a detailed parametric study of the blade pitch angle was conducted, revealing that the thrust coefficient increased with the pitch angle up to an optimal value. Beyond this point, the thrust coefficient decreased due to flow separation and stall, due to an excessive aerodynamic angle of attack. This analysis highlighted the importance of optimizing the pitch angle to maximize thrust generation and overall propeller efficiency.

In conclusion, the findings of this study have significant implications for the design and optimization of propellers in various applications, and highlighted the importance of efficient simulation setups in STAR-CCM+. These contributions offer valuable insights and practical guidelines for future propeller design and optimization efforts, advancing the field of rotor aerodynamics and CFD simulations.

6.2 Future works

The studies presented in this project serve as an initial point in the characterization of the aerodynamic performance of the experimental flat plate propeller. Thus, future working lines are proposed:

- Further characterization of the propeller performance by expanding the ranges and resolution of advance ratio and rotational speed analysed. This would give a complete vision of the aerodynamic performance involving flat plate propellers, allowing to comprehend with more detail the parameters that control the optimal aerodynamic behaviour.

- To repeat the different studies performed in this project employing a transient approach such as the RBM. This would allow to compare the validity of the pseudo-steady MRF approach, as well as to capture transient features that might be interesting to analyse.

- An aeroacoustic analysis of the propeller noise could be carried out to obtain the frequency spectrum and the sound pressure levels (SPL) produced by the propeller, employing a similar methodology to that of this project.

- Finally, it would also result interesting to perform an aeroelastic analysis, studying the different aeroeslastic instabilities, and the response of the structure and its vibrational modes.

Appendix A

Scope statement

A.1 Introduction

This chapter outlines the essential working conditions required for the successful development of the project while prioritizing personnel and equipment safety. The document distinguishes between the working environment and equipment conditions to ensure that both aspects are adequately addressed.

A.2 Working environment conditions

The workplace conditions should be optimised to enhance the productivity of workers while ensuring their well-being and the safety of equipment. Given that the entire project is carried out on a computer, the workplace's physical environment should adhere to the guidelines outlined in *Real Decreto 488/1997 de 14 de Abril* [31]. In summary:

To ensure a safe and comfortable work environment, it is imperative to provide adequate lighting and position the screen in a way that does not cause any harm to the worker's eyesight. The worktable should be spacious enough to accommodate all necessary equipment and allow for a comfortable working position. Furthermore, it should be sturdy enough to support the weight of the equipment. Lastly, the chair should be comfortable and promote proper posture by enabling adjustments to the height and inclination of the backrest.

In order to optimize work performance, it is important to ensure that the workspace is equipped with appropriate environmental conditions. An ideal workspace should possess a well-functioning ventilation system that facilitates frequent air circulation within the workspace. The temperature and relative humidity levels should be maintained within acceptable limits, with temperatures ranging from 21 ºC to 25 ºC and relative humidity levels ranging from 40% to 60%. Additionally, it is important to ensure that the equipment present in the workspace does not produce excessive noise that could potentially harm the worker's hearing or interfere with effective communication. Furthermore, it is necessary to minimize the levels of electromagnetic radiation outside the visible light spectrum to promote worker safety. Lastly, the software utilized in the workspace should be appropriate for the worker's level of knowledge and skill to ensure effective computer-person interaction.

A.3 Computer equipment specifications

The equipment employed for the project includes a laptop computer, which complies with the following specifications:

- Model: *Acer® Aspire 5*
- Processor: Intel® Core™ i5-8250U CPU (4-core, 1.60 GHz)
- RAM: 8 GB DDR4-SDRAM
- Storage: 1 TB SSD
- Graphics card: NVIDIA® GeForce® MX150, 2 GB VRAM
- Screen: 15.6”, 1366 x 768 px
- Power Supply: LiPo 48 Wh battery
- Operating System: Windows 10 64 bits

Table A.1 provides a list of the main software programs used, along with descriptions of their primary tasks.

Software	**Tasks**
MATLAB®	Numerical calculation, data processing, and graphing
Simcenter STAR-CCM+®	CFD and CSD-CFD simulations
Microsoft® Excel™	Simple calculations and results processing
Microsoft® PowerPoint™	Presentation and image creation
Overleaf	Document writing

Table A.1: Software utilized in the project

Appendix B

Budget

B.1 Introduction

This final chapter corresponds to the calculation of the economic value of the present Final Master's Degree Project. Firstly, the cost of the employed labour is computed; secondly, the cost of the computer equipment; and finally, an overhead rate is applied, which includes administrative costs and others not previously considered, as well as the Value Added Tax (VAT).

B.2 Labour Cost

The personnel involved include the author of the work (Junior Engineer), a doctoral student acting as co-supervisor (Engineer), and a Doctor in the faculty as supervisor (Doctor Engineer). The Final Master's Degree Project corresponds to a total of 13.5 ECTS credits. According to the current educational plan, each ECTS credit is equivalent to 25 hours of work, resulting in a total of 337.5 hours of work performed by the author, which are broken down as follows:

- Learning: 37.5 hours
- Project development: 200 hours
- Document writing: 100 hours

The salaries assigned to each engineer are, according to the Human Resources Service of the Universitat Politècnica de València, 30.82 €/h for the Senior Engineer; 18.28 €/h for the Engineer; and 13.7 €/h for the Junior Engineer. Thus, Table B.1 shows the total cost of labour.

B.3 Computer Equipment Cost

The various costs of the computer equipment can be divided into the amortization cost of the hardware employed and the cost of the software licenses utilized. The amortization cost is estimated as 20% per annum of hardware usage, based on the total acquisition price. Since the project development has progressed for 9 months, the amortization cost is computed for 0.75 years. Table B.2 shows the total amortization cost.

Concept	**Hours** [h]	**Cost per hour** [€/h]	**Cost** [€]
Junior Engineer	337.5	13.7	4,623.75
Engineer	30	18.28	548.4
Senior Engineer	30	30.82	924.6
Total			**6,096.75**

Table B.1: Total labour cost.

Acquisition price [€]	**Amortization coef.** [%/year]	**Years of use**	**Cost** [€]
800	20	0.75	120
Total			**120**

Table B.2: Hardware amortization cost

Among the software utilized, *Overleaf*, the online LaTeX editor, is the only free to use. *Simcenter STAR-CCM+*®, has an annual cost of 20,000 € and allows the use of 20 licenses simultaneously, of which 2 *Power on Demand* licenses were required for the completion of this project. As for the remaining programs, an annual license cost is assumed by the Universitat Politècnica de València for: *MATLAB*®, 800 €, and *Microsoft Office*®, 69 €. Thus, assuming 4,000 hours of average annual use, the total cost of the software employed in the development of this project is computed according to the hours of use per program described below. The breakdown of the total cost of the computer equipment is shown in Table B.3.

- Use of *MATLAB*®: 80 hours
- Use of *Microsoft Office*®: 50 hours

Concept	**Cost** [€]
STAR-CCM+®	2,000
Overleaf	0
MATLAB®	16
Microsoft Office®	0.86
Hardware A.C.	120
Total	**2,136.86**

Table B.3: Total computer equipment cost

B.4 Total Budget

Ultimately, the total project cost is calculated in Table B.4. 15% overhead and administrative cost rate is added, along with the corresponding 21% VAT.

Concept	**Cost** [€]
Labor cost	6,096.75
Computer equipment cost	2,136.86
Overhead costs (15%)	1,235.04
Subtotal	9,468.65
VAT (21%)	1,988.42
TOTAL	**11,457.07**

Table B.4: Total project cost

The total estimated cost of the Final Master's Degree Project above described and developed amounts to ELEVEN THOUSAND FOUR HUNDRED FIFTY-SEVEN EUROS AND SEVEN CENTS #**(11,457.07 €)**#.

Appendix C

Sustainable Development Goals

C.1 Introduction

In 2015, the United Nations established the Sustainable Development Goals (SDGs), a collection of 17 interconnected global goals designed to achieve a better and more sustainable future for all by 2030. These goals address a wide array of global challenges, including poverty, inequality, climate change, environmental degradation, peace, and justice. They serve as a universal call to action for governments, businesses, and civil society to work collaboratively towards sustainable development.

This chapter examines how the present project aligns with and contributes to the SDGs. By integrating the principles of sustainable development, the project aims not only to address immediate objectives but also to contribute to long-term global sustainability.

C.2 Relationship of the project with the SDGs

Table C.1 shows the degree of relationship of the project with the Sustainable Development Goals of the 2030 Agenda for Sustainable Development. The degree of relationship is indicated by marking each goal on a scale from High, Medium, Low or Not Applicable (N/A).

- **Goal 4. Quality education.** This project provides valuable knowledge and advancements in the field of rotor aerodynamics. The results may be used by researchers, engineers, and students to enhance the understanding of aerodynamic principles applied to propellers and rotors.

- **Goal 7. Affordable and clean energy.** Improving the propulsive efficiency of propellers contributes to more efficient energy use, reducing the demand for fossil fuels and promoting cleaner energy sources.

- **Goal 8. Decent work and economic growth.** Research in the aerodynamic performance of propellers may promote job creation in high-tech sectors and foster sustainable economic growth.

- **Goal 9. Industry, innovation and infrastructure.** The project is related to technological innovation and contributes to the development of more efficient transportation and energy infrastructures.

- **Goal 12. Responsible consumption and production.** Optimizing the performance of propellers can reduce resource consumption and waste generation.
- **Goal 13. Climate action.** Similarly to Goal 7, improving the propulsive efficiency reduces CO_2 emissions and contributes to climate change mitigation.

Sustainable Development Goals	**High**	**Medium**	**Low**	**N/A**
Goal 1. No poverty				[X]
Goal 2. Zero hunger				[X]
Goal 3. Good health and well-being				[X]
Goal 4. Quality education		[X]		
Goal 5. Gender equality				[X]
Goal 6. Clean water and sanitation				[X]
Goal 7. Affordable and clean energy			[X]	
Goal 8. Decent work and economic growth	[X]			
Goal 9. Industry, innovation and infrastructure	[X]			
Goal 10. Reduced inequalities				[X]
Goal 11. Sustainable cities and communities				[X]
Goal 12. Responsible consumption and production			[X]	
Goal 13. Climate action			[X]	
Goal 14. Life below water				[X]
Goal 15. Life on land				[X]
Goal 16. Peace, justice and strong institutions				[X]
Goal 17. Partnerships for the goals				[X]

Table C.1: Degree of relationship of the project with the Sustainable Development Goals.

Bibliography

[1] Y. Hu, "Two dimensional numerical simulation of cycloidal propellers with flat plate airfoil in hovering status," in *2013 International Powered Lift Conference*. DOI: `10.2514/6.2013-4244`. [Online]. Available: `https://arc.aiaa.org/doi/abs/10.2514/6.2013-4244`.

[2] S. Gaggero and D. Villa, "Steady cavitating propeller performance by using openfoam, starccm+and a boundary element method," *Proceedings of the Institution of Mechanical Engineers, Part M: Journal of Engineering for the Maritime Environment*, vol. 231, no. 2, pp. 411–440, 2017. DOI: `10.1177/1475090216644280`.

[3] L. Wang, J. Martin, M. Felli, and M. Carrica, "Experiments and cfd for the propeller wake of a generic submarine operating near the surface," *Ocean Engineering*, vol. 206, p. 107 304, Jun. 2020. DOI: `10.1016/j.oceaneng.2020.107304`.

[4] X. Liu, D. Zhao, and N. L. Oo, "Comparison studies on aerodynamic performances of a rotating propeller for small-size uavs," *Aerospace Science and Technology*, vol. 133, p. 108 148, 2023, ISSN: 1270-9638. DOI: `https://doi.org/10.1016/j.ast.2023.108148`.

[5] J. Xu, J. Yu, X. Lu, Z. Long, Y. Xu, and H. Sun, "Aerodynamic performance and numerical analysis of the coaxial contra-rotating propeller lift system in evtol vehicles," *Mathematics*, vol. 12, no. 7, 2024, ISSN: 2227-7390. DOI: `10.3390/math12071056`. [Online]. Available: `https://www.mdpi.com/2227-7390/12/7/1056`.

[6] Airbus, *Cityairbus nextgen. fully-electric and integrated urban air mobility*, Accessed: June 28, 2024. [Online]. Available: `https://www.airbus.com/en/innovation/low-carbon-aviation/urban-air-mobility/cityairbus-nextgen`.

[7] U. S. AirForce, *Mq-1b predator*, Accessed: June 28, 2024. [Online]. Available: `https://www.af.mil/About-Us/Fact-Sheets/Display/Article/104469/mq-1b-predator/`.

[8] DJI, *Phantom 4 pro v2.0*, Accessed: June 28, 2024. [Online]. Available: `https://www.dji.com/es/phantom-4-pro-v2`.

[9] A. Chambon, "Analyse aéroélastique expérimentale et analytico-numérique de pales de rotor flexibles," Doctoral Dissertation, Institut Supérieur de l'Aéronautique et de l'Espace, 2023.

[10] A. Cremades, "Fluid-structure interaction with the application to the non-linear aeroelastic phenomena," Doctoral Dissertation, Universitat Politècnica de València, 2023.

[11] J. Anderson, *Computational Fluid Dynamics*, 3rd ed., W. J.F., Ed. Berlin: Springer, 2009, ISBN: 978-3-540-85056-4. DOI: `10.1007/978-3-540-85056-4_1`.

[12] NASA, *Navier-stokes equations*, Last accessed: 2022, May 16. [Online]. Available: `https://www.grc.nasa.gov/www/k-12/airplane/nseqs`.

[13] O. Reynolds, "An experimental investigation of the circumstances which determine whether the motion of water shall be direct or sinuous, and of the law of resistance in parallel channels," vol. 174, pp. 935–982, 1883.

[14] R. Rosa, "Turbulence theories," in *Encyclopedia of Mathematical Physics*, J.-P. Françoise, G. L. Naber, and T. S. Tsun, Eds., Oxford: Academic Press, 2006, pp. 295–303, ISBN: 978-0-12-512666-3. DOI: `https://doi.org/10.1016/B0-12-512666-2/00111-5`.

[15] S. Pope, *Turbulent Flows*, Ed. by C. U. Press. Cambridge: Cambridge University Press, 2009.

[16] Altair, *Turbulence scales and energy cascade*, Accessed: May 15, 2024. [Online]. Available: `https://help.altair.com/hwcfdsolvers/acusolve/topics/acusolve/training_manual/turb_scales_energy_cascasde_r.htm`.

[17] P. Martí, "Apuntes de ampliación de mecánica de fluidos," *Editorial Universitat Politècnica de València*, 2018.

[18] P. Spalart, W. Jou, M. Strelets, and S. Allmaras, "Comments on the feasibility of les for wings, and on a hybrid rans/les approach," Jan. 1997.

[19] P. Spalart and S. Allmaras, "A one-equation turbulence model for aerodynamic flows," in *30th Aerospace Sciences Meeting and Exhibit.* DOI: `10.2514/6.1992-439`. [Online]. Available: `https://arc.aiaa.org/doi/abs/10.2514/6.1992-439`.

[20] H. Versteeg and W. Malalasekera, *An Introduction to Computational Fluid Dynamics: The Finite Volume Method.* Longman Group Ltd, 1995, ISBN: 978-0-582-21884-5.

[21] F. R. Menter, "Two-equation eddy-viscosity turbulence models for engineering applications," *AIAA Journal*, vol. 32, no. 8, pp. 1598–1605, 1994. DOI: `10.2514/3.12149`.

[22] J. Anderson, *Fundamentals of Aerodynamics*, 5th ed. McGraw-Hill Education, 2010, ISBN: 978-0-073-39810-5.

[23] H. Schlichting and K. Gersten, *Boundary-Layer Theory*, 9th ed. Springer, 2017, ISBN: 978-3-662-52917-1. DOI: `10.1007/978-3-662-52919-5`.

[24] NuclearPower, *Boundary layer*, Accessed: May 24, 2024. [Online]. Available: `https://www.nuclear-power.com/nuclear-engineering/fluid-dynamics/boundary-layer/`.

[25] A. Bayón, *Wall functions. introdution to cfd*, Accessed: May 25, 2024. [Online]. Available: `https://cfd.blogs.upv.es/turbulence/wall-functions/`.

[26] R. Courant, K. Friedrichs, and H. Lewy, "On the partial difference equations of mathematical physics," *IBM Journal of Research and Development*, vol. 11, no. 2, pp. 215–234, 1967. DOI: `10.1147/rd.112.0215`.

[27] SimFlow, *Courant number in cfd*, Accessed: May 22, 2024. [Online]. Available: `https://sim-flow.com/courant-number-in-cfd/`.

[28] J. G. Leishman, *Principles of Helicopter Aerodynamics*, 2nd ed. Cambridge University Press, 2006, ISBN: 978-0-521-85860-7.

[29] W. Johnson, *Helicopter Theory.* Dover Publications, 1994, ISBN: 978-0-486-68230-3.

[30] M. Hepperle, *Aerodynamic characteristics of propellers*, Accessed: May 14, 2024. [Online]. Available: `https://www.mh-aerotools.de/airfoils/propuls3.htm`.

[31] R. D. 488/1997, *14 de abril, sobre disposiciones mínimas de seguridad y salud relativas al trabajo con equipos que incluyen pantallas de visualización*, Boletín Oficial del Estado n.97, de 23 de abril de 1997.